1990ApJ...355...70C

THE ASTROPHYSICAL JOURNAL, 355:70–87, 1990 May 20

IMAGING SPECTROPHOTOMETRY OF IONIZED GAS IN NGC 1068.
I. KINEMATICS OF THE NARROW-LINE REGION

GERALD CECIL
Institute for Advanced Study

AND

JONATHAN BLAND AND R. BRENT TULLY
Institute for Astronomy, University of Hawaii

Received 1989 July 5; accepted 1989 November 29

ABSTRACT

We have used an imaging Fabry-Perot interferometer and CCD at the University of Hawaii 2.2 m telescope to synthesize [N II] $\lambda\lambda$6548, 6583 emission-line profiles with ($<1''$, $\sim$140 km s^{-1}) FWHM (spatial, velocity) resolution across the inner $1'$ diameter of the nearby Seyfert galaxy NGC 1068. The stack of monochromatic images spatially resolved the high-velocity gas ($\sim 6''$ radius and $\sim$3000 km s^{-1} line widths) and has been extensively analyzed for kinematic and photometric content. Our profiles agree well with previous long-slit work, but their complete spatial coverage has now allowed us to constrain the gas volume distributions. We find that the narrow-line region (NLR) is distributed in a thick (FWHM $\sim 3''.3 = 230$ pc) center-darkened, line-emitting cylinder that envelopes the collimated radio jet. The cylinder is composed of three distinct kinematic subsystems, which we discuss.

1. High-velocity gas emits 75% of the total dereddened narrow-line region (NLR) [N II] flux (corresponding to a mass of $\sim$38,000 [$10^{4.5}$ cm$^{-3}/n_e$] $M_\odot$, with n_e the mean electron density). A kinematic model consistent with the data is used to argue that this gas fills the cylinder with two families of nested cones of increasing opening angle in the NE and SW quadrants. The maximum opening angle may be as large as 150°. The axial inclination to the line of sight in the NE is 75°, so the cylinder axis is inclined $\sim$45° to the disk plane. The brightest high-velocity flux in the NE is concentrated in the conical shell with opening angle $\sim$82°. The shell is thick, with Gaussian dispersion $\sim 3''.3 = 230$ pc FWHM perpendicular to the cone axis. The emitting filaments are optically thick, with $A_V \sim 1.3$ mag of internal extinction. Line-of-sight velocities are approximately proportional to $r^{0.6}$ (with r the cylindrical radius from the jet axis), and so are roughly those of a constant-speed conical outflow. Intrinsic gas velocities deproject to $\sim$1500 km s^{-1} with respect to systemic velocity, and we infer an average mass loss of $\sim$0.15 [$10^{4.5}$ cm$^{-3}/n_e$] $M_\odot$ yr^{-1}. The large extranuclear line widths in this NLR apparently arise from geometrical projection and spatial averaging of an asymmetric, large-scale flow, with no evidence for intrinsic "turbulence" in the outflowing filaments. The filaments are too massive ($\geq 10^{-2}$ $M_\odot$) to be broad-line region (BLR) clouds blown to resolvable radii. We argue instead that molecular clouds with average density $\sim 10^{2.5}$ cm^{-3} are forced by the stellar bar (prominent in near-IR images) from $10''$ radius into the inner NLR, where they are exposed to a high-speed (0.1c) nuclear wind whose kinetic luminosity is similar to the ionizing luminosity of the nucleus. Fragments stripped by fluid instabilities are crushed to densities of $\sim 10^3$–10^5 cm^{-3} during their wind acceleration, but they are stable to conductive thermal evaporation in the hot shocked wind for masses and velocities derived from our spectra.

2. Gas near systemic velocity is concentrated in a narrow kinematic feature brightened along the boundaries of the NE radio lobe. It accounts for 8% of the total NLR [N II] flux (corresponding to $\sim 1.2 \times 10^5$ [10^3 cm$^{-3}/n_e$] $M_\odot$), but negligible kinetic energy. This component is also apparent in Hα images and so represents a mass enhancement rather than an excitation effect. Its deprojected velocity deviates by less than 175 km s^{-1} from the bar-forced flow field defined by gas in the large-scale disk. The only significant velocity deviation (80 km s^{-1} along the line of sight) is localized in an expanding "ripple" around the base of the NE lobe at $\sim 3''$ radius, with no associated flux enhancement.

3. Nine percent of the total NLR [N II] flux (corresponding to $\sim$1000 [10^5 cm$^{-3}/n_e$] $M_\odot$) is emitted by a component which dominates within $1''$ radius and extends $2''$ along $\sim$100° P.A. Its centroid is blueshifted by $\sim$270 km s^{-1} from systemic, and it has line width $\sim$600 km s^{-1} (i.e., typical of a Seyfert 2 galaxy). The brightest flux from this component apparently arises in spatially unresolved kinematic substructure that is associated with the nuclear triple radio-source ($\sim 0''.7$ extent). Our highest resolution images show a tight correlation between the brightest line emission and the radio source, in agreement with speckle line imaging.

Subject headings: galaxies: individual (NGC 1068) — galaxies: internal motions — galaxies: jets —
galaxies: Seyfert — interferometry

I. INTRODUCTION

Ionized gas ranging over velocities of several thousand km s^{-1} is found several arcseconds outside the nuclei of a few nearby active galaxies. Emission line profiles in these so-called narrow-line regions (NLRs) can show abrupt spatial variations, suggesting that multiple kinematic subsystems are projected on the line of sight. An NLR frequently coincides in scale and orientation with a "linear" distribution of nonthermal radio emission (Wilson 1987, 1988), plausibly representing a low-luminosity variant of the collimated "jet" outflows in radio galaxies (Wilson and Ulvestad 1982). The discrete components in the line profiles might then arise from radiative shocks in either the ambient interstellar medium (ISM) or the outflow ejecta (e.g., Wilson 1989, and references therein). Alternatively, the radio structure may represent only one manifestation of a more extensive thermal outflow. Our aim has been to mitigate one limitation of previous observational attempts to clarify the dynamical linkage between radio and line-emitting substructures, namely the incomplete spatial coverage of long-slit spectrographs on the complex gas distribution. Our Fabry-Perot data cubes were obtained with a CCD in sub-arcsecond seeing, cover the *entire* spatially extended NLR of NGC 1068, and they clearly resolve line-emission counterparts to radio-continuum structures in this nearby (14.1 Mpc; Tully 1988) Seyfert galaxy. We argue that a high-speed thermal wind blows through this NLR and accelerates interstellar clouds (Schiano 1985, 1986); the wind is more extensively distributed than the radio flux.

A prominent ellipse of H^+ regions delineates the classical NLR (Fig. 1, Pl. [3]) at an average radius of 13″ (0.9 kpc). The ellipse is actually the ionized outer edge of a massive molecular ring that partially circumscribes the NLR (Myers and Scoville 1987, hereafter MS; Kaneko *et al.* 1989). Considerable dust attenuates optical line emission within this ring (Young, Kleinmann, and Allen 1988). At smaller radii, bright optical emission lines (Bertola 1966; Balick and Heckman 1985) of high ionization (Pogge 1988) and velocity align with a jet/double-lobed radio source (Condon *et al.* 1982; Wilson and Ulvestad 1983, 1987, hereafter WU83, WU87). While the ionized NLR is composed of a great number of individual kinematic subsystems which appear uncorrelated on a scale of ~75 pc (Atherton, Reay, and Taylor 1986), four spatially extended, kinematically distinct high-velocity "cloud" complexes dominate the energetics (Walker 1968). Long-slit kinematic studies have focused on these structures: Alloin *et al.* (1983, hereafter APBS) decomposed the line profiles into Gaussian components and tracked component variations along two position angles over several arcseconds; Baldwin, Wilson, and Whittle (1987, hereafter BWW) presented spectra of high signal-to-noise ratio and ~100 km s^{-1} resolution at many points across the NLR; Meaburn and Pedlar (1986, hereafter MP) have obtained two echelle spectra at 10 km s^{-1} resolution that show Walker's clouds in great detail. WU83 suggested that jets are interacting with the NLR gas and have subsequently (WU87) modeled the NE radio lobe as an ejecta-driven bow shock in the ambient ISM

We obtained detailed kinematic data to study the outflow/ISM interaction; their reduction is outlined in § II. This section is rather long and many readers may wish to skip to § III, where we identify structures both spatially in channel maps and kinematically in grids of our synthesized spectra. We isolate kinematic subsystems in the line profiles (including Walker's clouds) and constrain their energetics. We briefly consider possible dynamical explanations in § IV and summarize our conclusions in § V.

II. IMAGING SPECTROPHOTOMETRY

a) Data Acquisition

Most previous kinematic studies of this NLR have employed the bright, spectrally unblended [O III] λ5007 line, which has high contrast relative to emission from H^+ regions. Our study of NLRs is an outgrowth of our interest in high-velocity gas flows in lower luminosity systems (e.g., Cecil 1988), where the most prominent circumnuclear emission line is often [N II] λ6583, with [O III] of comparatively small equivalent width atop a composite stellar continuum. The optical performance of our present etalon degrades sharply at shorter wavelengths, so we have restricted our scans to the [N II], Hα complex. This has two consequences. First, lines are strongly blended near the nucleus, so we must forego study of Hα at radii less than 3″. The [N II] profile must be constructed by abutting the blue wing of [N II] λ6548 to the red wing of [N II] λ6583. Problems at the telescope meant that the blue wing of λ6548 was covered with only nine exposures. To synthesize the blue wing, these channels were combined with four others blueward of systemic velocity on the λ6583 line. Comparison of our data set with the long-slit spectra of BWW and MP shows that, despite our crude velocity sampling of the blue wing, we have captured the important kinematic substructure.

The second consideration is the periodic wavelength transmission of an etalon. Spectral orders are confused if the intrinsic width of the emission line under study is broader than the interorder free-spectral range (FSR). The etalon employed in the Fabry-Perot study of Atherton, Reay, and Taylor (1986) was unsuited to a study of NLR kinematics because its small FSR would have produced hopeless interorder confusion. We therefore use a high-finesse etalon with 4000 km s^{-1} (85 Å) FSR, in the 75th order. The bandpasses of our order-separation filters are smaller than the FSR to prevent contamination by the continuum, and the filter transmission profile is flat-topped to ensure accurate line synthesis. We critically sampled the [N II] and Hα emission lines at 60 km s^{-1} increments, an acceptable procedure here because the high-velocity substructure within the line profiles is broader than this over most of the classical NLR.

We acquired two data sets. We discuss here the [N II] data cube obtained on 1985 October 14 (red wing) and October 15 (blue wing) with the Hawaii Imaging Fabry-Perot Interferometer (HIFI; Bland and Tully 1989) and a low-noise ($6e^-$ rms readout when operated as here without preflash, and ~40% quantum efficiency at Hα) GEC CCD (McKay 1986). This instrument was attached to the standard Cassegrain focus of the University of Hawaii 2.2 m telescope, whose effective *f*-ratio was reduced to *f*/8.6 (corresponding to a pixel scale of 0″.24) for these observations. Thirty-one 5 minute exposures (for a total exposure of 155 minutes) sampled the red wing of [N II] λ6583 from −180 to 1600 km s^{-1} at 60 km s^{-1} increments.[1] Nine 7 minute exposures of [N II] λ6548 erratically sampled its blue wing from 0 to −1000 km s^{-1} (relative to systemic). Finally, on 1986 October 25 17 samples were obtained of the Hα line. These profiles are not well sampled, so images from our Hα cube served only to define the emission-line morphology of the NLR (e.g., Fig. 1). Comparison of the profiles in Figures 3 and 4 of BWW show that Hβ and collisionally excited profiles are grossly similar.

Our second data set covers [N II] λ6583 and Hα and was obtained at the facility Fabry-Perot interferometer (Boulesteix *et al.* 1983) of the 3.6 m Canada-France-Hawaii telescope (CFHT), with a less favorable pixel scale for high-resolution

---

[1] Velocities quoted are *relative to the systemic value of the galaxy*, 1150 km s^{-1} (MP). Velocity dispersions have been corrected in quadrature for the Airy instrumental profile of the etalon (which is effectively a Gaussian with 65 km s^{-1} FWHM). All images have north at top, east at left.

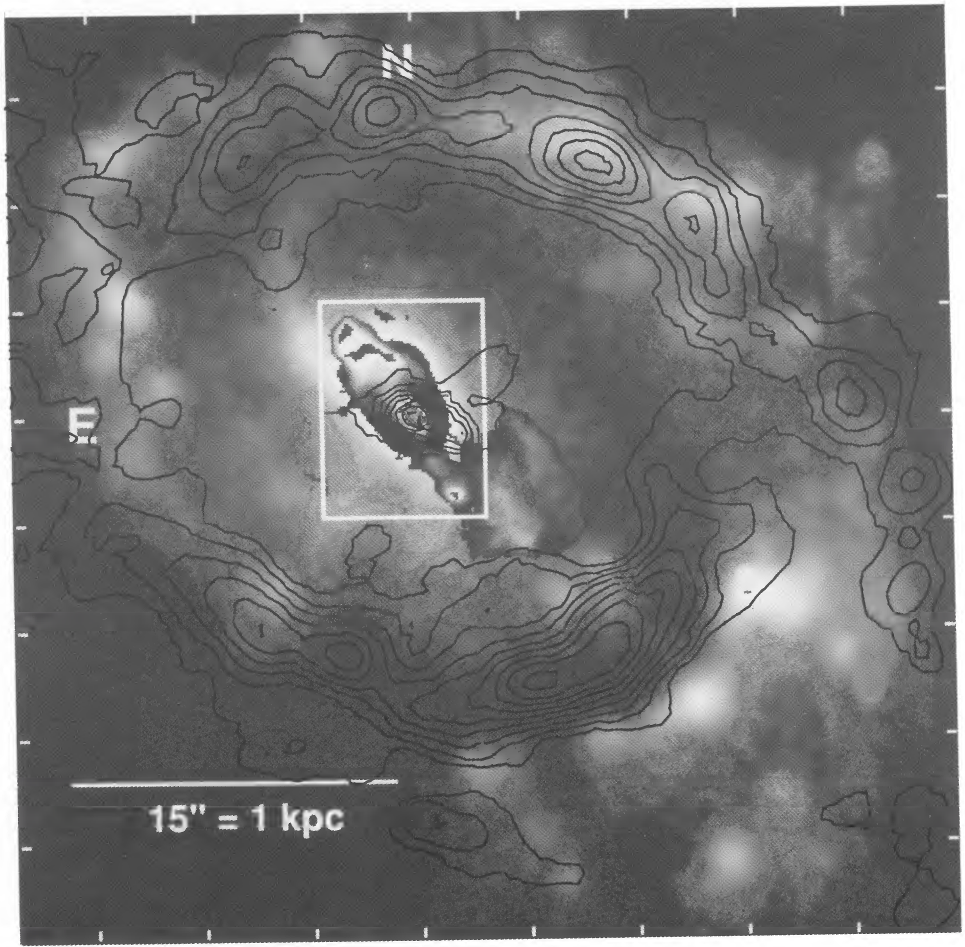

FIG. 1.—The NLR of NGC 1068, circumscribed by a broken ring of H^+ regions, is shown in this single 5 minute CCD exposure through the HIFI system on the University of Hawaii 2.2 m telescope; ticks every 5″. Hα emission, extending over a 65 km s^{-1} (FWHM) extent centered on the systemic velocity of NGC 1068, is shown in 1″ seeing (FWHM), together with the log of the λ-6 cm continuum (Wilson and Ulvestad 1983). The CO flux (Planesas, Scoville, and Myers 1989) is contoured on top. Spectra in Fig.3*a* are extracted from the boxed region.

CECIL, BLAND, AND TULLY (*see* **355**, 71) study (0$''$.43) but at an effective *f*-ratio of 2 and a velocity resolution of 85 km s^{-1}. This data set is sensitive to emission of lower surface brightness and has been used to study both the large-scale kinematics of the gaseous disk, and the kinematic and spatial dependence of the extranuclear [N II]/Hα flux ratio. The latter distribution can constrain mechanisms that excite the ionized gas. These data are discussed elsewhere (Bland, Cecil, and Tully 1990, hereafter Paper II), but were used here to convert our [N II] spectra to an absolute flux scale. The [N II]/Hα ratio map derived from the CFHT cube was used to bootstrap recombination fluxes from our [N II] spectra, in order to constrain the masses, and hence energetics, of the kinematic subsystems isolated in our [N II] profiles. The CFHT data were also used to establish kinematic links between the NLR and surrounding large-scale disk (Paper II). The emphasis of the present paper is strictly on the brightest line emission at radii less than 10$''$.

We used a CCD detector to maximize sensitivity and dynamic range. Because these devices have finite readout noise, we integrated for a single 5 minute exposure at each etalon spacing, requiring one night to sample the entire line wing down to a typical 3 σ specific intensity of 10 mJy arcsecond^{-2}. Such slow-scan Fabry-Perot observations are susceptible to transparency and seeing variations. Ideally these are monitored with a field star in each frame, but unfortunately there are no suitable stars in the 2.2 m data cube. However, simultaneous 10 μm photometry by the United Kingdom Infrared Telescope (UKIRT) in the same region of the sky judged the conditions photometric on both nights, and we were able to synthesize reliable profiles.

We will show that the sharpest frames partially resolve optical line emission associated with the triple nuclear radio source, whose outer two elements are separated by 0$''$.7 in the λ-2 continuum (Ulvestad, Neff, and Wilson 1987). Fits to spatially unresolved H$^+$ regions show that the seeing was $\leq$0$''$.9 FWHM (60 pc) at all velocities where it could be measured (i.e., those near systemic). Because successive frames were acquired at large velocity displacements from one another and then interleaved, small seeing variations about this value do not introduce serious systematics. Seeing variations are apparent in the line profiles only where the spatial gradient of the emission line flux is large. This slight channel-to-channel fluctuation is effectively removed when the spectra are individually smoothed with a one-dimensional Hanning filter. Figure 2 shows typical [N II] λ6583 channel maps whose extent define the classical NLR at the velocities shown. The extranuclear stellar continuum is minor compared to the intense line emission from the NLR.

b) *Data Cube Calibration*

i) *Spatial and Photometric Registration*

Data were calibrated and analyzed with locally developed software on the network of Sun 3 work stations at the Institute for Advanced Study. In outline, the reduction sequence is as follows (see Bland and Tully 1989 for a more detailed discussion). The debiased frames were first stacked into data cubes. Dome flat-field frames had been taken over a full free-spectral range to map the transmission profile of the order separation filter (effective central wavelength of 6615 Å at 0° C in *f*/8.6 converging beam and 50 Å passband). This so-called white-light cube served to correct both for pixel-to-pixel sensitivity variations and for modulation of the line profiles by the intrinsic transmission profile of the order-separation filter. Because color sensitivities of individual pixels on the CCD are not expected to vary over the limited wavelength range that we scan, the high-pass filtered flat-frames were co-added to improve signal statistics. The result was divided by the sum of the smoothed flats, and this normalized flat was in turn divided into each data frame. The filter response at each pixel was removed by dividing the Gaussian smoothed white-light cube into the data cube. The white-light cube was not spatially smoothed prior to this division, because we do not attempt to correct for low-frequency inhomogeneities in the filter transmission.

The data were then spatially registered by interpolating with bicubic splines, assuming that line emission peaks at the nucleus at all velocities. MP find that the peak of the [O III] λ5007 line flux is offset 0$''$.6 NE from that of the visual stellar continuum. Our interframe registration is defined by the N$^+$ channel at 600 km s^{-1}, which shows a line emission analog of the nuclear radio triple. This permits registration of our data cube to within one pixel (0$''$.24) of the radio continuum. However, our limited velocity coverage makes it difficult to establish a reliable continuum level for spectra within $\sim$2$''$ radius, so we cannot address the reported (MP) offset between line and continuum peaks.

The blue wing profiles were spline-interpolated to the same velocity resolution as the red, and the two data sets were aligned and merged. The synthesized [N II] profiles were Hanning smoothed to clean up residual pixel-to-pixel fluctuations, resulting in a FWHM of 140 km s^{-1}. Finally, profiles were binned 2 × 2 to critically sample the average seeing.

These data were acquired while our instrumentation and observational methodology were being refined, and in consequence several complications came to light during calibration. The passband of our transmission filter was not optimally matched to the kinematic structure of NGC 1068, resulting in noticeable flux attenuation at the extreme blueward channels of the red wing. The profile restoration was initially poor for these channels because residual charging in the substrate of our unthinned CCD led to offsets of $\sim 7e^-$ above the nominal value of the electrical bias, and this spurious positive mean caused the filter restoration to overcompensate. Subtraction of the average offset prior to restoration solved the problem and led to well-behaved profiles at most pixels. The extreme red channels (i.e., channels of lowest flux) show residual intensity fluctuations in regions of low surface brightness, apparently caused by a deferred charge problem with the CCD readout. This baseline uncertainty limits our kinematic decompositions to the region covered by the classical NLR. Isovelocity surfaces are nested paraboloids in our data cubes (and skewed, because the etalon was tilted by a few degrees relative to the optical axis to displace ghost images off the detector). We have ignored this well-defined velocity gradient because it has similar magnitude to our velocity sampling over the subcube considered in this paper. The data are contaminated by spurious charge spots that were later found to originate from the slightly radioactive faceplate of the CCD dewar (MacKay 1986). These spots and cosmic-ray hits are easily eradicated with a running median filter of three adjacent channels when the cube is processed as an array of spectra.

We converted our [N II] data to an absolute flux scale by referencing it to our calibrated [N II], Hα cube from the CFHT. (Accurate fluxes could be obtained from field stars in

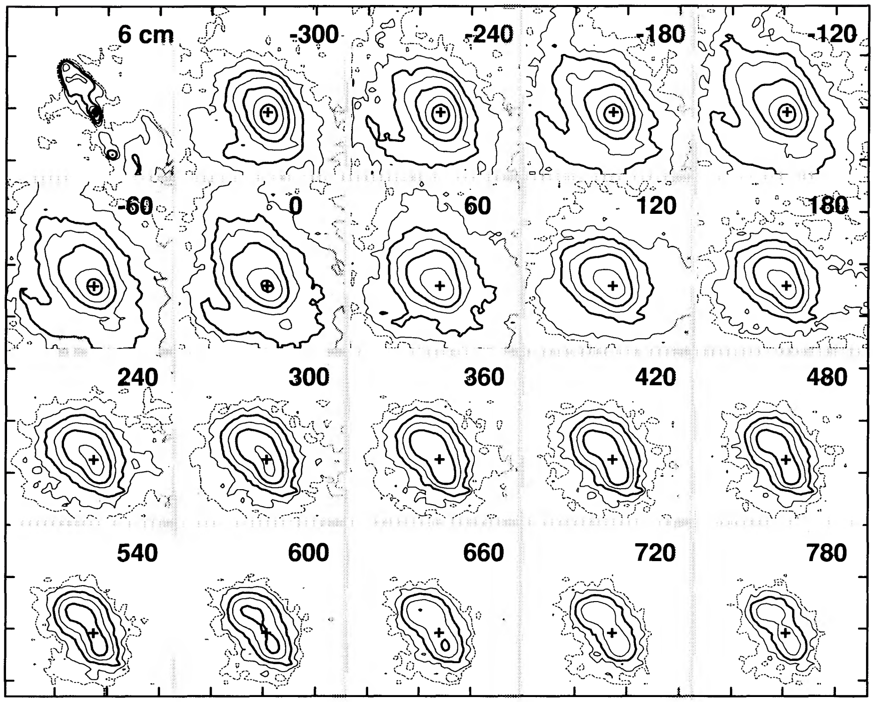

FIG. 2*a*

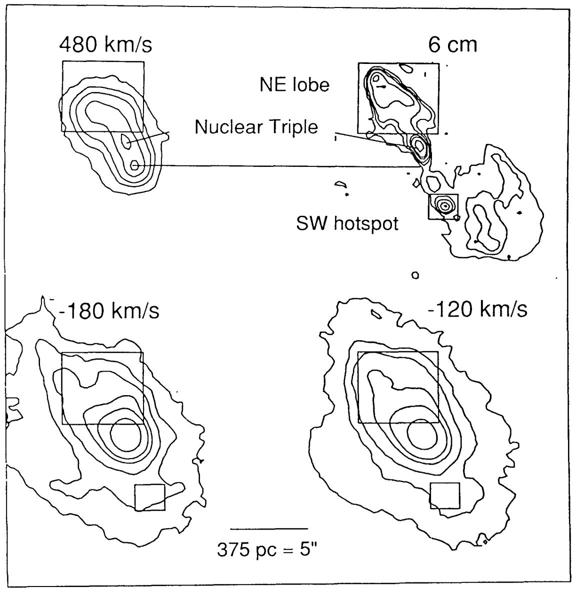

FIG. 2*b*

FIG. 2.—(*a*) 65 km s^{-1} slices (FWHM) through the [N II] λ6583 emission line. The log of the λ-6 cm continuum is shown in the upper left-hand corner, at the same scale and orientation. Ticks at 5" intervals. The stellar continuum and nuclear component (§ III*a*[iii]) have been subtracted. Velocities are relative to systemic (1150 km s^{-1}: Meaburn and Pedlar 1986). Line-emission contour levels increase by factors of 2 from 10 mJy arcsecond^{-2}. The nuclear position is marked with a " +." Note the "linearization" of the NLR as the velocity increases above systemic, and edge brightening of the NE lobe at velocities near systemic. (*b*) Boxes outline regions of correspondence between optical line and radio continuum structures. The optical images have FWHM 65 km s^{-1}, centered at the velocities shown.

the latter cube, which are not present in the more restricted field of the 2.2 m data set. The brightnesses of these stars were, in turn, measured with respect to a primary standard [Hayes 1970].) Mean atmospheric extinction corrections, appropriate for that epoch at the Mauna Kea Observatory (Pierce 1987), were applied.[2] The two cubes were spline interpolated to similar spatial and spectral grids, the line profiles were compared in the region of wavelength overlap, and the relative intensity transformation was derived. Slight differences at intermediate flux levels were apparent and can be attributed to the superior spatial resolution of the 2.2 m data cube. Differences were also apparent at low flux levels, in excess of those expected from shot noise, which arose from the charge transfer problem mentioned above. These effects are negligible in the CFHT data cube because of the different detector used (Texas Instruments 500^2 CCD) and the increased sky flux in larger pixels at *f*/2. The spectrum at each pixel was therefore rescaled so that the velocity-integrated intensity agreed with that of the interpolated CFHT cube. This correction is small and has only

---

[2] At low northern latitudes in 1985 October *R*-band extinctions were increased 0.04 mag by the El Chichon volcanic plume. The stratosphere had recovered by 1987 January.

a minor effect on the derived fluxes. Our total [N II] λ6583 flux of 1.5×10^{-11} ergs cm^{-2} s^{-1} is in excellent agreement with that of others (Shields and Oke 1975: 1.2×10^{-11} ergs cm^{-2} s^{-1} in 3″.5 radius, using an average ratio [N II] λ6583/Hα ∼ 2.3 [Paper II]; Koski 1978: 1.3×10^{-11} ergs cm^{-2} s^{-1} through a 2″.7 × 4″.0 slit).

ii) *Reddening Correction*

Most studies find moderate reddening to the nucleus ($E_{B-V} = 0.5$, corresponding to $A_V \sim 1.5$ mag for a standard reddening curve [e.g., Miller and Mathews 1972]). At larger radii, Bergeron, Petitjean, and Durret (1989) derive $E_{B-V} \sim 1$ in the region of high-velocity gas. Young, Kleinmann, and Allen (1988) have attempted to quantify the influence of dust by ratioing flux-calibrated, narrow-band [S III] λ9532 and Hα images and comparing the result to the unreddened value of ∼0.5 (empirically derived from galactic H^+ regions). The use of [S III]/Hα as a reddening estimator has been criticized by Kennicutt and Pogge (1990). An alternate way to increase the [S III]/Hα ratio is to heat the [S III]–emitting gas with the nuclear continuum and perhaps also with relativistic electrons/cosmic-ray particles associated with the jet. Spectroscopic studies (e.g., BWW, and references therein) have demonstrated that the NLR excitation/ionization conditions are not those of H^+ regions, so it is plausible that the NLR [S III]/Hα ratio is increased over the value found in normal H^+ regions. Evidently, Brackett line imaging will be required to improve estimates of the extranuclear reddening. Faced with these uncertainties, we chose $E_{B-V} \sim 0.5$ as typical of the inner NLR. Despite the likely presence of distributed dust within emitting filaments (see § IV*b*), we assumed no scattering and the standard galactic reddening curve. In the following we show the profiles as observed, but we quote dereddened fluxes in our discussion of gas parameters.

The data cubes were thus assembled into ∼1200 flux-calibrated spectra at 0″.5 increments across the NLR. Repre-

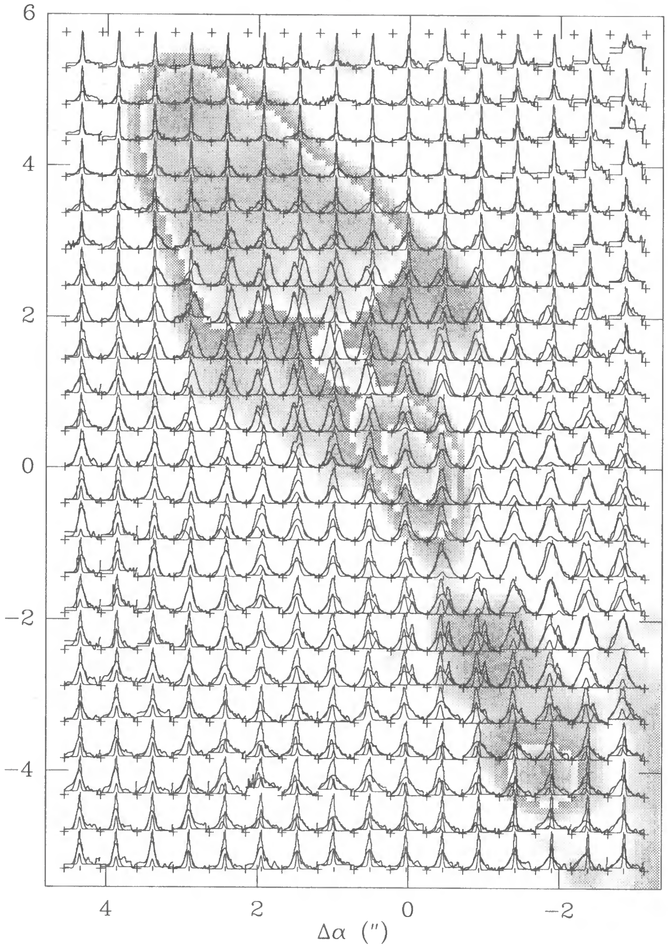

FIG. 3*a*

FIG. 3.—(*a*) Normalized and continuum-subtracted emission-line profiles synthesized from a stack of 36 5 minute exposures of [N II] λ6583 and nine 7 minute exposures of [N II] λ6548. Profiles are binned 2 × 2 (i.e., 0″.5 square), scaled at each point to suppress the hundredfold decrease in absolute surface brightness across the region shown, and plotted on the log of the λ-6 cm continuum. The tick marks systemic velocity in a total range of 3200 km s^{-1}. Spectra have been Hanning smoothed to ∼140 km s^{-1} resolution and median-reject filtered to excise spurious charge spots. Profile decompositions into one, two, or three Gaussians are superposed. Maps of selected Gaussian parameters are shown in Fig. 5. (*b*) Rotated [N II] data cube, plotted on the log of the λ-6 cm continuum. The nuclear component of each profile has been subtracted (see § III*a*[iii]). Profiles are shown both autoscaled at each point and globally scaled to preserve flux variations across the NLR; each is plotted in a box 0″.5 square and 3200 km s^{-1} extent. Vertical bars denote midpoints and horizontal bars denote the extents of the spectral sequences plotted in Fig. 4. [O III] λ5007 profiles from the long-slit spectra of BWW are overplotted to show similarity with [N II]; these are averaged over 1″.5 square and plotted over 4300 km s^{-1} extent.

1990ApJ...355...70C

sentative spectra are shown in Figure 3*a*, referenced to the λ-6 cm continuum map of WU83. As we will discuss shortly, patterns in the channel maps suggested that the jet axis is an important symmetry axis for the distribution and kinematics of ionized gas. To decouple flux and kinematic variations, we therefore rotated our data cube by 30° to align it with the radio jet (Fig. 3*b*). Spectra and their spatial derivatives, extracted in swaths perpendicular to the jet axis, are plotted in Figure 4.

c) *Comparison of Our Line Profiles with Previous Work*

Most kinematic structure in our synthesized [N II] spectra agrees well with that of the [O III] λ5007 long-slit spectra of MP and BWW at points of intersection, demonstrating that slow-scan, CCD-based Fabry-Perots can generate emission-line profiles of long-slit quality on a pixel-by-pixel basis. The advantage of a Fabry-Perot is, of course, that we map profiles over an extended area $\sim$100 times faster than with even multislit spectroscopy.

Glaspey, Walker, and Stockton (1975) and Pelat and Alloin (1980, hereafter PA) decomposed the integrated [O III] profile into several cloud systems, including those mapped by Walker (1968). Walsh (1983) confirms these systems. APBS improved spectral and spatial constraints, both studies showing that the most prominent spatially extended features in the NLR are: a broad ($\sim$1700 km s^{-1} FWHM) structure with $n_e < 10^7$ cm^{-3} that apparently extends to radii of $\sim 1''$ (component B in the notation of PA); a structure of FWHM $\sim$600 km s^{-1} which is centered near systemic and which is responsible for most of the flux in the inner few arcseconds radius (component 4); a narrow feature near systemic velocity (component 5, hereafter the "flare") that extends NE to radii of at least 6″; and Walker's high-velocity clouds (components 2, 3, 6, and 7). A minor component on the extreme blue wing (component 1) extends to $\sim 1\farcs4$ radius NE (MP). It is likely responsible for the blue-wing asymmetry of the "nuclear" component (§ III*a*[iii]), and it will not be further discussed.

These features are obvious in our profiles. Figure 4 plots several spectral cuts across the NLR, together with their spatial derivatives to summarize local flux and velocity variations. Our data and the long-slit profiles of BWW show that throughout the NE quadrant (and beyond the EW boundaries of the radio lobe) the "flare" sits atop a broad base whose velocity centroid is usually redshifted from systemic (Fig. 4*a*). MP report faint wings which span $\sim$200 km s^{-1} on [O III] profiles in the NE quadrant at radii up to 40″. This structure is evidently too faint for detection in our *f*/8.6 data cube but was detected at the CFHT and is discussed in Paper II. Our spectra and those of BWW and MP show that clouds I and III of Walker are visible as double peaks in the profiles just NE of the nucleus (Fig. 4*d*). Both features are obvious in the echelle spectra of MP, centered at $1\farcs4$ NE radius. South-west of the

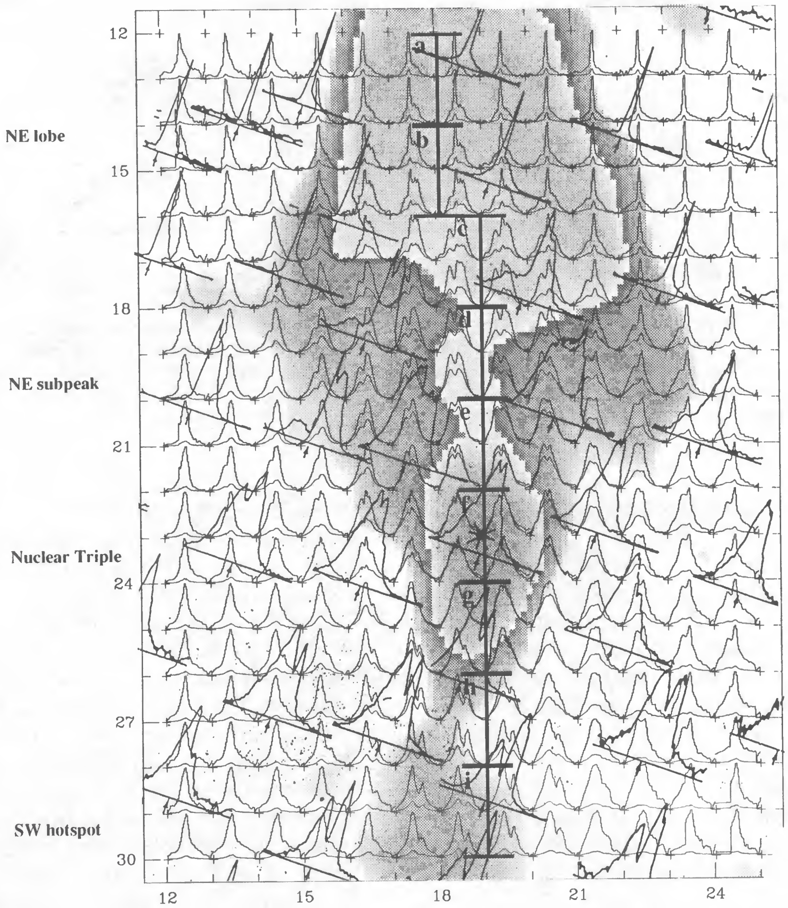

FIG. 3*b*

1990ApJ...355...70C

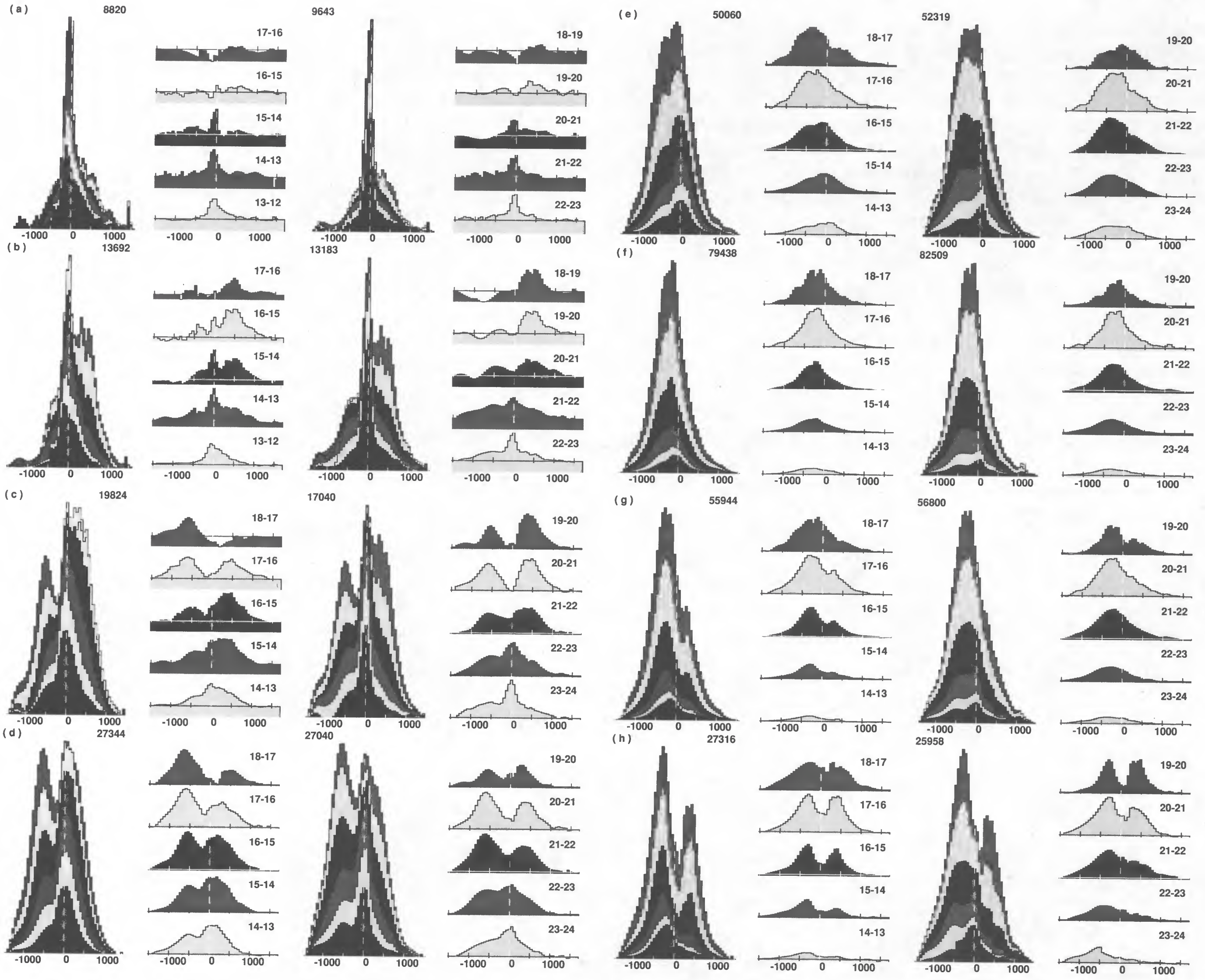

FIG. 4.—Sequences of [N II] spectra along directions perpendicular to the radio axis, at the points shown between the bars in Fig. 3*b*. Continuum-subtracted spectra are extracted in boxes (1″, 0″.5) (across, along) the jet axis, and overplotted with relative fluxes preserved. The maximum flux in each box is shown, in arbitrary units. Plots are paired across the jet axis with the left-hand member of each pair in the eastern half and the right-hand member in the western. So the jet axis lies between increments 17 and 18. Ticks along the horizontal axes are at 500 km s^{-1} increments; the dashed vertical white line marks systemic velocity. Difference profiles (right-hand side of each plot) are shaded in the gray scale of the brighter spectrum in the differenced pair.

nucleus, clouds II and IV of Walker (1968) are visible as double peaks in all data sets (Fig. 4*h*).

Line widths exceed 3000 km s^{-1} at several points in the NLR. The broad recombination line profiles observed by Antonucci and Miller (1985; see also Bailey *et al.* 1988) in polarized light have intensity roughly 1% of the nuclear line flux, with no broad [O III] component observed at this level. The high-velocity components of the [N II] profiles in the NE quadrant are substantially brighter, indicating no detectable scattered flux from an inner NLR. (This is not surprising in the scattering configuration proposed by Krolik and Begelman 1986, because scattering is then effective only in regions dense enough for complete collisional de-excitation of [N II].) So our profile variations reflect *in situ* emissivity changes. The intensities of the high-velocity components decrease a hundredfold across the NLR, requiring the large dynamic range of a CCD to track their variation. We note that [O III], Hβ, and [N II] profiles are in general quite similar, although there are differences in the relative amplitudes of discrete, kinematic components within the profiles. In particular, the (blue, red) wings (NE, SW) of the nucleus have (higher, lower) excitation. In detail, our [N II] profiles agree better with the Hβ profiles, although Balmer absorption undoubtedly affects the latter.

Our profile decompositions are summarized in § III. They complement those of PA in that we suppress details of the nuclear spectrum and concentrate on large-scale kinematic features over the entire NLR. At small radii, our velocity coverage is insufficient to follow the line flux down to the stellar continuum, which was determined independently of the fits described below using the median of the line-free part of the spectrum. This baseline uncertainty complicates extraction of the broad component from our line profiles and may account for some of the differences to be discussed in § III between our kinematic decomposition and that of APBS.

d) *Line Profile Analysis*

Striking patterns exhibited by the brightest emission in our channel maps constrain the kinematic organization of this NLR. They indicate that the gas flow is *organized*, not chaotic, when projected on the line of sight. Hence there is a strong *geometric* component to the gas distribution that must be understood and removed from the profiles before a dynamical analysis is possible. This section describes how we parameterized the kinematic subsystems in our data cube. In § III we isolate and map the spectral and spatial extents of these parameters. In § IV these maps are effectively interpreted as different physical regimes that arise in the ISM when it interacts with a supersonic outflow.

Figure 4 shows that the gas distribution exhibits four distinct kinematic domains: in the upper half of the NE radio lobe, the narrow kinematic "flare" dominates (Fig. 4*a*); near the base of the NE lobe, the profiles are double-peaked and broad (Figs. 4*c*, 4*d*); near the nucleus, the profile is dominated by a bright, moderately broad component slightly blueshifted from systemic velocity (Fig. 4*f*); and SW of the nucleus, the profiles are again double-peaked (Fig. 4*h*). Walker (1968) first noted that such line splitting across the nucleus is consistent with biconal outflow. We will quantify this geometry in § III. For now, note from the difference spectra that seemingly complex variations often arise from the combined effects of only one or two kinematically distinct subsystems whose individual velocity structure is adequately described by a Gaussian (see also APBS). At many locations, differencing the profiles successfully isolates a kinematic subsystem because the other components are relatively constant. This regularity is the key to disentangling the line profiles. Once we isolated a component by differencing, the profiles were decomposed at each point by fits with constrained velocity centroids and, occasionally, fixed dispersions to stabilize and direct the optimization procedure.

The kinematic decomposition that emerges from our analysis differs from those of APBS and PA. They attributed much of the line flux to a single broad component (~ 1700 km s^{-1} FWHM). Our more extensive spectra and those of MP and BWW show that the blue and red wing variations are decoupled, even within 1″ of the nucleus, which would require dramatic and implausible point-to-point centroid shifts of a single broad component. By splitting this component into separate blue and red wings NE of the nucleus, we can naturally account for such variations, and by their convergence, we can account for the observed dispersion decrease of the broad profile base as the edges of the NE lobe are approached.

A complication is that the number of components we isolate in a profile depends on the signal-to-noise ratio of the spectrum. In many locations, a narrow component near systemic velocity sits atop a broad base of high-velocity material. While we could estimate fluxes of high- and low-velocity material in these regions, we could not reliably parameterize kinematics of the broader component. Even in regions of comparatively high signal-to-noise ratio, covariance between the different fit parameters causes low-amplitude, point-to-point variations in the dispersion, flux centroid, and continuum maps. However, these unphysical spatial variations are inconsistent with the atmospheric seeing, and so they were suppressed by averaging adjacent points in the parameter maps. We then refit the line profiles with the dispersion, centroid, and continuum parameters now fixed at their smoothed values, but with the amplitudes allowed to vary. Spatial continuity of our maps is disrupted when, because of diminished signal-to-noise ratio, we shift our decomposition tactics from two symmetric wings to a single broad component. However, such regions contribute little to the velocity-integrated flux of each component. Furthermore, our aim was simply to parameterize the data cube content, not to physically motivate a Gaussian basis.

Finally, Hα fluxes, masses, and therefore "turbulent" (representing spatially unresolved substructure) energies of each component of the parameterized profile can be obtained by bootstrapping dereddened recombination fluxes from the local [N II]/Hα ratio. In § IV*a*, we establish the geometry of the high-speed outflow in the NE quadrant of the NLR, and we deproject the velocity field to derive kinetic energies of the outflow in the galaxy rest frame.

III. EMPIRICAL RESULTS

a) *Kinematic Subsystems*

Figure 2 shows a subset of the monochromatic N^+ channel maps. Figure 2*a* reproduces the λ-6 cm A-array VLA map of WU83 on the same scale and shows that the brightest parts of the optical line and radio continuum emission distributions coincide in spatial extent and orientation, a characteristic exhibited by many other Seyfert galaxies (Wilson 1988). Our kinematic decomposition of the emission-line profiles reveals a detailed correspondence between individual kinematic subsystems and different parts of the radio structure (Fig. 2*b*).

i) *High-Velocity Emission*

At radii less than 5″, the most striking pattern exhibited by the NLR (Fig. 2) is its *linearization along the jet axis with increasing velocity, on both sides of the nucleus at once*. This trend extends over a 450 km s^{-1} range and is most pronounced at 480 km s^{-1} (Fig. 2). In the 480 km s^{-1} image, the line flux is distributed $\sim 4\overset{''}{.}5$ along the linear part of the radio jet; it has a constant transverse FWHM of $1\overset{''}{.}3$ (corrected for seeing, ~ 90 pc) along its length, and it fades abruptly when the radio jet flares into the NE radio lobe and SW hotspot. If this pattern is dynamically significant, we might reasonably expect it to appear as a feature in the line profiles (Fig. 3). We therefore tagged those channels in the red wing of [N II] λ6583 that show linearization and find that away from the nucleus, this pattern corresponds to Walker's clouds I and II, NE and SW of the nucleus, respectively. The blue wing shows grossly similar behavior, producing twin-peaked profiles over the region of linearization. This splitting is masked within a few arcseconds of the nucleus by an additional kinematic component (number 4 of PA; discussed in § IV*a*[iii]) that is projected along the line of sight. This is obscured in the velocity-integrated flux map because multiple subsystems often overlap spatially. Once this component is removed by fitting (Fig. 3*b*), it becomes clear that the linear pattern in the monochromatic images (Fig. 2*a*) is a combination of this component and discrete lobes of high-velocity emission NE and SW of the nucleus.

Our data constrain the emitting volume as follows:

1. The high velocities associated with linearization (i.e., significantly above escape) and the precise orientation along the jet axis argue that we are seeing a nuclear outflow. That the flux distribution linearizes on *both* sides of the nucleus in the *same* channel implies that the outflow is not restricted to the axis of the bidirectional jet, but must have a strong component

of motion *perpendicular* to the jet axis, for example as in a wide cone. The ionization ratio [O III]/([N II] + Hα) is conically distributed in the NE quadrant (Pogge 1988).

2. Difference spectra perpendicular to the linear jet show that most flux is augmented in the line wings (i.e., Walker's clouds I and III), at velocities up to ± 1250 km s^{-1} relative to systemic (Figs. 4*c*, 4*d*). The centroids of this flux-change converge to systemic velocity as the line of sight moves from the jet axis through the boundary of the radio lobe. (Note that convergence occurs *beyond* the radio boundary, at radii $> 2''$.) This pattern is also consistent with cylindrical or biconal expansion. Line profiles are also double-peaked SW of the nucleus, in the region of a radio hot spot. Fits show that the peaks shift by ~ 150 km s^{-1} toward systemic off axis, but the convergence point is indeterminant with our data because the line wings fade rapidly.

3. In the NE quadrant, red and blue profile wings have similar dispersions, supporting our contention that they are part of a single dynamical structure. However, they have different emission distributions, kinematics, and excitation ratios. Whereas the red wing extends to the tip of the NE lobe, the blue vanishes at the lobe center. In cylindrical symmetry, the emission of front and back volumes of the NE quadrant then differ. Both components fade with increasing radius.

4. In regions of split profiles, the relative strengths of blue and red wings in the difference spectra are similar, arguing for constant external extinction across the line emitting volume. However, in the original spectra the (red, blue) wing is always stronger in the (NE, SW) quadrant.

5. At many points our [N II] profiles are similar to the [O III] and Hβ profiles of BWW (Fig. 3*b*).

Using these regularities to constrain our decomposition, we optimized the amplitude of the flare, and the centroids, amplitudes, and common dispersion of the wings. Parameterization and data are compared in Figure 3*a*. Figure 5 maps several parameters derived from our profile decomposition. Figure 6 plots flux profiles of the high-velocity component along and across the jet axis.

Between $2''.5$–$5''.5$ radii, we find broad profile bases (FWHM ~ 1200 km s^{-1}) similar to those on the [O III] profiles (BWW). Beyond $\sim 2''.5$ east of the jet axis, our profiles have broader bases than provided by the sum of two Gaussians, unlike the double-peaked [O III] profiles. Some of this difference arises from the comparatively low signal-to-noise ratio of our poorly sampled blue wings. However, it also reflects real changes in gas excitation, hence internal filament structure.

ii) *Emission Near Systemic Velocity*

In Paper II we show that the large-scale velocity field of the ionized gas is symmetric across the nucleus. This is *not* the case in the NLR (Fig. 5*d*). Evidently, the regular motions in the SW quadrant of the NLR are distorted by an additional component in the NE that we are unable to isolate in our profiles because of their inadequate velocity resolution. Echelle spectra (MP) in the NE quadrant split the profile into two components separated by ~ 50 km s^{-1} (see also APBS). One component is contiguous with the large-scale disk (APBS), which we argue in Paper II is strongly responding to the stellar bar (Thronson *et al.* 1989) in NGC 1068. If we assume that its flux is similar to that in the SW quadrant, we find that it accounts for $\sim \frac{1}{3}$ of the total flux in the NE. (This estimate is certainly no better than a factor of 2 because the kinematic modeling required to remove the underlying bar response is nontrivial and beyond the scope of this paper.)

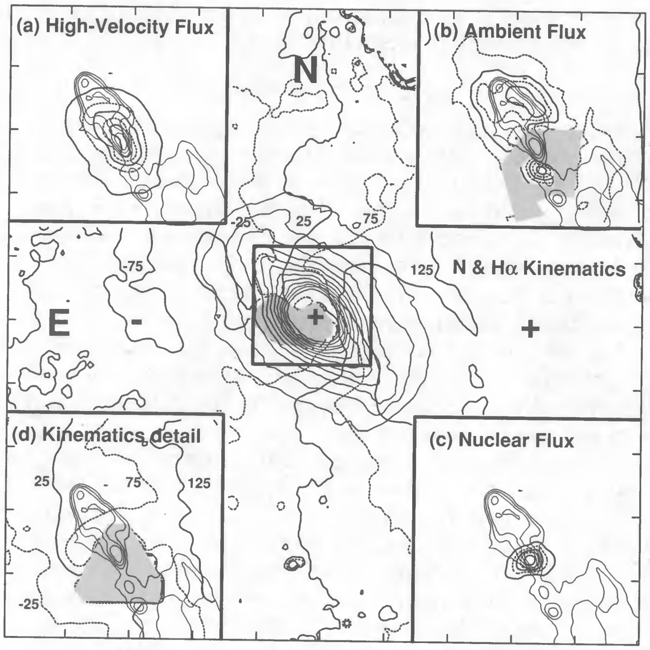

FIG. 5.—Kinematic subsystems in the NLR of NGC 1068. (*Main figure*) The large-scale disk kinematics in [N II] and Hα within $44''$ (3 kpc) radius (see Paper II); contours are relative to the systemic velocity. Solid and dashed lines alternate. We find a (kinematic major axis, disk inclination) of (90°, 35°), respectively. The Z-shape in the center is characteristic of a bar-forced gaseous disk; the 2.2 μm continuum image of the stellar bar is contoured on top. The boxed region ($17'' = 1.1$ kpc square) is enlarged in inserts (*a*)–(*d*), which plot distributions of component flux ([*a*]–[*c*]; log scale, contours double) and velocity centroid ([*d*]; linear scale). Strongly blended profiles could not be decomposed in the gray areas. The log of the λ-6 cm continuum is also shown. Ticks at $9''$ ($5''$) increments in the main figure (inserts). (*a, upper left*) High-velocity gas accounts for most of the NLR mass and kinetic energy, with $\sim \frac{3}{4}$ of it tightly aligned with the linear part of the radio jet. Symmetries in the NLR profiles and monochromatic images suggest conical expansion of gas about the jet, with deprojected velocities ~ 1500 km s^{-1}. Cuts along and across this distribution are plotted in Fig. 6. (*b, upper right*) Ambient ISM interacting with the expanding radio lobes. Material is found: (*a*) NE of the nucleus in a narrow-velocity (< 60 km s^{-1} FWHM) feature, and (*b*) in an optical hotspot with somewhat broader lines, at the southern end of the linear part of the radio jet. In detail, both features are edge brightened along the leading side with respect to galactic rotation. The bright knot on the jet axis SW of the nucleus coincides with a local minimum of the radio continuum. (*c, lower right*) The nuclear component has FWHM ~ 600 km s^{-1} and extends along 100° P.A. (*d, lower left*) Kinematic response of the gaseous disk to the nuclear outflow. The "ripple" across the base of the NE radio lobe (80 km s^{-1} maximum difference) is the only strong deviation from the large-scale, bar-forced flow.

The remaining flux is distributed across the NE radio lobe (Fig. 5*b*) as the "flare" discussed by PA (component 5) and MP. It is often responsible for most of the flux change in our difference spectra (e.g., Fig. 4*a*). It attains greatest intensity along the western boundary of the NE lobe; Hα images show similar brightening, so this is a mass enhancement rather than an excitation effect. While this is the leading side of the lobe in the sense of galactic rotation, so ambient disk gas may have piled up against the expanding radio structure, the ram pressure of gas in the large-scale disk is hard to establish because this gas is likely rotating in elliptical not circular orbits (Paper II).

Useful constraints are provided by the relative constancy of the flare kinematics, despite strong variations in both the

1990ApJ...355...70C

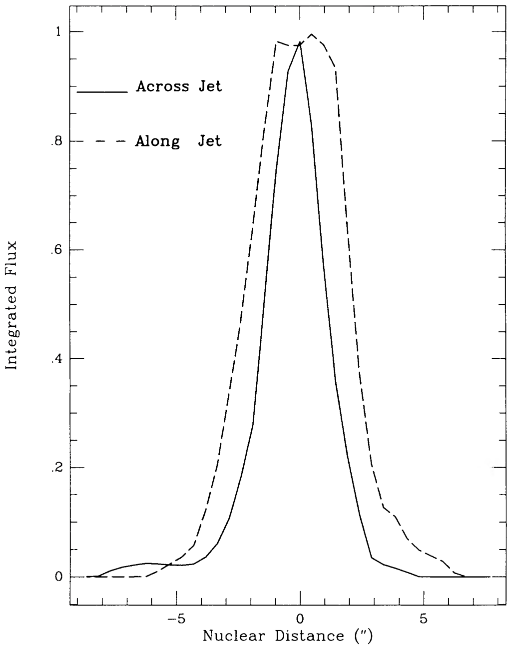

FIG. 6.—Profiles of the high-velocity line emission averaged over (2″, 5″) (along, across) the linear part of the radio jet. The resolved Gaussian FWHM across is 1″.75. Negative distances span the (NE, SE) quadrant (along, across) the jet.

intensity (Nishimura, Kaneko, and Toyama 1984; BWW) and [O III]/(Hα + [N II]) ionization ratio (Pogge 1988). Figure 5*b* shows that gas kinematics in the upper half of the lobe deviates by ≤ 40 km s^{-1} from the large-scale disk flow. The strongest deviation is ~ 80 km s^{-1}, across the base of the NE lobe; it accounts for 20% of the total near-systemic flux. Although the high-velocity component fades rapidly through this region, requiring a switch from three- to two-Gaussian decomposition, the flare is still isolated in the difference spectra and the ripple is a strong pattern, so we are confident of its reality. The ionization structure of high- and low-velocity gas flows also differ: APBS note that the flare has ratio [O III]/H$\beta \sim 17$ compared to ~ 7 for the rest of the line, so it is experiencing a significantly larger ionization parameter (consistent with gas density $\ll 10^{4.5}$ cm^{-3} and the observed nuclear spectrum that extends to soft X-rays [Bergeron, Petitjean, and Durret 1989]). The apparent weakness of the ionization and kinematic coupling argues that the two regions are geometrically distinct, but projected along the same line of sight.

iii) *Nuclear Component*

Within $\sim 1''$ radius, flux is augmented in the nuclear component (number 4 of PA). Difference spectra near the nucleus at various position angles show that this is spatially extended (e.g., Fig. 4*f*), as suggested by PA and confirmed by APBS, with the low-level flux addition distributed symmetrically EW about the nucleus. The elongation is roughly perpendicular to both the axis of the high-velocity emission and the bar shocks traced outside the NLR. We determined its extent by fixing its velocity centroid and dispersion and setting the dispersions of the NE wing components equal as before. The fits show that it has FWHM ~ 550 km s^{-1}, centroid blueshifted ~ 270 km s^{-1} from systemic, and is extended along $\sim 100°$ P.A. (Fig. 5*c*). Its line width is $\sim 1\ \sigma$ from the distribution mean for [O III] $\lambda 5007$ in active galactic nuclei (AGNs) (Wilson and Heckman 1985), considerably larger than the nuclear stellar velocity dispersion ($\sigma = 150$ km s^{-1}; Richstone and Morton 1975). Presumably our near-nuclear profiles still blend several compact kinematic subsystems, including the obvious asymmetry in their blue wings (component 1 of PA) that is not incorporated in our parameterization. Individual images further constrain the flux distribution of these components. The brightest flux in the 600 km s^{-1} image coincides in extent, outline, and orientation with the triple nuclear source studied in detail with radio VLBI by Ulvestad, Neff, and Wilson (1987) and mapped in speckle reconstructions of the [O III] $\lambda 5007$ line by Ebstein, Carleton, and Papaliolios (1989). Evidently the gas distribution is tightly correlated with the VLBI source at the seeing limit, and we expect a view through the *Hubble Space Telescope* similar to Figure 2 of Ulvestad, Neff, and Wilson (1987).

The complexity of the nuclear profile means that our constraints on its rotation are loose, less than ± 130 km s^{-1}. For comparison, the rotation due to a compact nuclear mass $M_H \approx 1.5 \times 10^7\ M_\odot$ (as estimated from luminosity arguments by Krolik and Begelman 1986) is 30 km s^{-1} at $1''$ (70 pc) radius.

b) *Physical Parameters of the Ionized Gas*

i) *Gas Densities*

Shields and Oke (1975) derive S$^+$ and O$^+$ densities of ~ 800 cm^{-3} but obtain $\sim 2 \times 10^5$ cm^{-3} for the velocity-integrated [O III] $\lambda 5007$ nuclear profile from constraints on the Ar^{3+} density and O^{++} temperature. Walsh (1983) subsequently argued that the higher density is appropriate for all kinematic components of the nuclear profile except the narrow flare. The average density must be of this order or less because our nuclear [N II] profile resembles the [O III] profile of MP and Walsh (1983) (once we account for our lower velocity resolution), and so has suffered little collisional quenching [$n_{\rm crit}$([N II] $\lambda 6583) \sim 9 \times 10^4$ cm^{-3}]; for this reason, the value 10^7 cm proposed by PA is certainly too high. Shields and Oke (1975) developed photoionization models of the nuclear region and fit their spectra most effectively with a composite of both densities wherein 40% of the [O III] flux comes from a time-dependent component with $n_e \sim 800$ cm^{-3}. Because the gas emissivity increases strongly with density, this implies that most of the [O III] emitting material is at densities below 10^5 cm^{-3}. These, and subsequent models which include the important charge-exchange reactions, generally require at least two zones to fit spatially integrated profiles of many NLR line-species (Koski 1978; Carroll and Kwan 1983, hereafter CK). In fact, we argue in § IV*c* that the emitting filaments are wind confined and accelerated. There is then a continuous density range in the NLR, with $n_e(R) \geq 10^{2.5}$ cm^{-3}. We take the average density across the inner NLR of $10^{4.5}$ cm^{-3}, but we emphasize that the uncertainty in this value is a major limitation to current discussions of the NLR dynamics. It is obviously important to obtain reliable estimates of the Ar^{3+} density. The kinematic continuity of the flare with the large-scale disk argues that its density is more typical of diffuse structure. We therefore assume $n_e \sim 10^3$ cm^{-3} for this and other diffuse emission, consistent with estimated S$^+$ and O$^+$ densities.

ii) *Ionized Masses*

We derive masses from our [N II] data in two ways: by bootstrapping recombination fluxes, and directly from the [N II] $\lambda 6583$ flux. In both approaches, we parameterize mass in terms of both the NLR temperature (because it is unclear what heats the ionized gas), and density which, as we have just shown, is poorly constrained by standard plasma diagnostics. We first assume full ionization with case B recombination, and therefore underestimate the total mass of optically thick filaments. To establish Hα fluxes, we divided our dereddened [N II] fluxes by the velocity-averaged [N II]/Hα ratio map derived in Paper II from the CFHT data cube. (There we show that the ratio has a velocity-dependent component, but for our present purpose this influence is small.) The ionized mass is then

$$M \approx 144\, L_{40} \frac{2.3}{F_{[\mathrm{N\,II}]}/F_{\mathrm{H}\alpha}} \frac{T_4}{n_{e,5}} M_\odot \;,$$

where L_{40}, T_4, and $n_{e,5}$ are the line luminosity (in units of 10^{40} ergs s^{-1}), gas temperature (in 10^4 K), and gas density (10^5 cm^{-3}), respectively. Alternatively, we calculate the collisionally excited [N II] λ6583 population with the three-level approximation of McCall (1984). (This approximation agrees with a five-level treatment within 5%.) For solar nitrogen abundance, the ionized mass is then:

$$M \approx 149 L_{40} f(n_{e,5}\, T_4)/X\; M_\odot \;,$$

where $f(n_{e,5},\, T_4)$ is a rational function given in McCall (1984), and X is the N$^+$ ionization fraction. The excellent agreement with the recombination value shows that nitrogen is mostly in this state, provided it is not significantly overabundant in the NLR. The resulting masses and energies of each kinematic component are significantly higher than those found by PA, who apparently populated the [O III] $\lambda\lambda$4959, 5007 transitions from a single level.

Table 1 summarizes the physical properties of each component. Figure 7 shows their contribution to the spatially integrated [N II] NLR profile and should be compared to the nuclear [O III] profile plotted in Figure 3 of PA and Figure 2 of Walsh (1983). We observe fewer components with different relative strengths because of: (1) more precise discrimination possible with spatial resolution, (2) variations in the gas excitation, (3) our lower velocity resolution, and (4) our inclusion of angular sectors that were missed by PA. We estimate that the average linear mass density of expanding gas is ~100 $M_\odot$ pc^{-1} near the base of the NE lobe. This value of course applies only to gas at 10^4 K. Hotter gas in pressure equilibrium with this component may be of comparable mass, depending on its filling factor. Dense molecular clouds may also be present and indeed may form the NLR filaments (Schiano 1986).

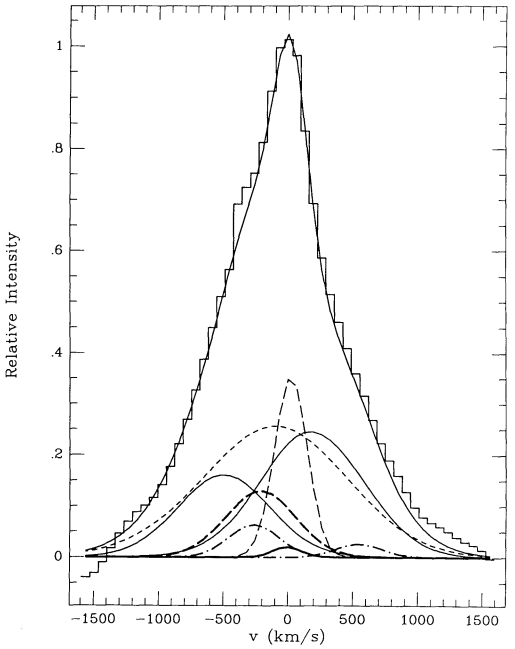

FIG. 7.—Summary of NLR kinematic content. [N II] profile arising from spatial integration over all points in the NLR where the kinematic decomposition into Gaussian components was possible. Individual components are shown, together with their sum and the sum of the original data. *Heavy dashed line:* nuclear component (9% of total NLR flux). *Thin solid lines and short dashed line:* NE wing and broad components (together, 75% of total NLR flux). *Long dashed line and heavy solid line:* components near systemic velocity (12% of total NLR flux). *Dot dashed lines:* SW high-velocity components. Compare this figure to the [O III] profile in Fig. 3 of PA80.

TABLE 1

PHYSICAL PARAMETERS OF THE IONIZED GAS

COMPONENT	PERCENTAGE OF NLR [N II] FLUX	[N II] 6583 FLUX Observed (10^{-12} ergs cm^{-2} s^{-1})	Dereddened[a] (10^{-12} ergs cm^{-2} s^{-1})	[N II] λ6583 / Hα	IONIZED MASS[b] ($M_\odot$)	ENERGIES Kinetic[c] (10^{52} ergs)	Turbulent[d] (10^{52} ergs)
Red wing	25	3.9	11.3	2.3	12,600	28[e]	...[e]
Blue wing	14	2.2	6.4	2.3	7000	16[e]	...[e]
Broad	36	5.6	16.2	2.3	18,000	...	13.3
Total HV	75	11.7	33.8	2.3	38,000	44	13.3
Nucleus[f]	9	1.2	3.8	3.0	1000	<0.01	0.1
Flare[g]	8	1.2	3.4	2.3	$\sim 1.2 \times 10^5$	0.3	0.2
SW hotspot	4	0.6	1.5	2.3	500	...	<0.01
Diffuse[g,h]	4	0.6	1.5	2.3	52,000	...	0.1
Total NLR	100	15.4	44.3	...	2.1×10^5	44.3	13.7

[a] Dereddened values using $E_{B-V} \approx 0.5$ (Koski 1978) and standard Whitford reddening curve (Miller and Mathews 1972).

[b] For case B recombination at $n_e \sim 10^{4.5}$ cm^{-3}, $T \sim 10^4$ K (Walsh 1983), and 14.1 Mpc distance (Tully 1988).

[c] Velocities relative to $V_{\mathrm{sys}} \sim 1150$ km s^{-1} (MP).

[d] Unresolved kinematic substructure, with $E_{\mathrm{turb}} = \frac{1}{2}M(3/2){v_{\mathrm{turb}}}^2$; $v_{\mathrm{turb}} = V_{\mathrm{FWHM}}/1.67$.

[e] Outflow velocities deproject to ~1500 km s^{-1} with respect to systemic velocity. Deprojection accounts for the "turbulent" contribution to this component.

[f] Assuming $n_e \sim 10^5$ cm^{-3}, $T \sim 10^4$ K (Shields and Oke 1975).

[g] Assuming $n_e \sim 10^3$ cm^{-3}, $T \sim 10^4$ K (Shields and Oke 1975).

[h] Sum of diffuse structure throughout NLR.

iii) *Radio Correlations and Anticorrelations*

Statistical samples of Seyfert nuclei show correlation between the spatially integrated $\lambda 21$ cm monochromatic radio power and both the luminosity and line width of [O III] $\lambda 5007$ (e.g., Wilson and Heckman 1985, and references therein). Figure 2*b* shows that the brightest high-velocity line emission is tightly aligned with the radio jet, while gas near systemic velocity is enhanced at the boundaries of the NE radio lobe. (Bright line emission coincident with radio flux in the middle of the lobe probably also lies along the boundary and is projected along the line of sight.) Evidently, correlations are preserved for individual kinematic subsystems. However, the kinematic deprojection discussed in § IV*b* makes it clear that the radio structure is embedded in a much more extensive outflow, with considerable high-velocity gas in regions of only faint radio emission. The clearest anticorrelation is the line-emitting knot SW of the nucleus that is projected on a local minimum of the radio jet. This feature is visible in several monochromatic images (e.g., Fig. 2*b*) and can be separated from the line profiles (Fig. 5*b*). Such optical/radio displacement was observed by Whittle *et al.* (1988) in their slit spectra of flows in other active galaxies, and was there identified with the postshock cooling length in the ambient ISM. In our case, it appears to be associated with a redirection of the jet flow after it leaves the nuclear triple. The line emission is displaced from the radio in the leading direction with respect to galactic rotation, so ram pressure from the ambient disk may be responsible (Wilson and Ulvestad 1982).

IV. DISCUSSION

The most striking patterns in our kinematic decomposition are:

1. High-velocity emission tightly aligned along the jet axis on both sides of the nucleus. The dereddened surface brightness corresponds to an average ionized mass density of ~ 100 $M_{\odot}$ pc^{-1} at the NE subpeak and base of the NE lobe. Kinetic energy and line widths are greatest there, and line emission fades rapidly through this region.

2. Low-velocity emission coincident with the NE radio lobe. Its flux and kinematic variations are anticorrelated: flux is edge-brightened along the lobe boundaries, yet the kinematics deviate by less than 50 km s^{-1} from the bar-driven flow field of the large-scale gas disk. The strongest kinematic deviation, ~ 80 km s^{-1}, occurs at the base of the NE lobe where the high-velocity filaments disappear; there is no associated flux change.

The collisionally excited line profile at each point in the NLR depends on the electron densities, and the volume occupied by filaments of a range of electron and ion densities and radial velocities (e.g., Wilson and Heckman 1985). As these authors note, a model line profile at each point in the flow requires specification of the gas ionization (to relate ion to electron densities) and a dynamical model describing the time dependence of each filament's volume. We argue below that the filaments are optically thick. Each therefore emits $F_c = \epsilon_c(n_c) A_c N_{\rm uv}/R^2$ photons per second, where A_c is the filament area, R is its distance to the nucleus emitting $N_{\rm uv}$ ionizing photons per second, and the emissivity for collisionally excited lines $\epsilon_c \approx n_c{}^2$ for densities below critical deexcitation and $\approx n_c$ above. We now constrain these parameters to the extent practical from flux maps of a single, collisionally excited emission line; only the long-slit [O III] observations of BWW are available to complement our observations. Our analysis is further limited by the uncertain average emitting gas density. Luminosity uncertainties due to poor constraints on extranuclear reddening are less significant.

a) Filament Structure

High-velocity gas is distributed throughout a cylinder of length and radius $\sim 5''$ (370 pc). The observed mass of $\sim 38{,}000$ $M_{\odot}$ at $n_e \sim 10^{4.5}$ cm^{-3} is there clumped into what are usually visualized as isolated "clouds" or filaments; an alternative topology is discussed in § IV*c*[ii]. The low filling factor ($\sim 10^{-8}$) shows that each clump is exposed to the full ionizing flux of the nucleus (luminosity $L_{44} \sim 10^{44}$ ergs s^{-1}; Krolik and Begelman 1986). A reliable estimate of column densities (and hence mass spectra) would constrain the filament physical structure and means of acceleration. Unfortunately, in this NLR the columns are poorly constrained by the very limited extranuclear coverage of diagnostic lines (principally [O I] $\lambda 6300$) that are formed in the partially ionized zone (PIZ) of each filament. Large [Ne V]/He^{+} ratios at $10''$–$50''$ radii (Bergeron, Petitjean, and Durret 1989) show that soft X-rays photoionize the NLR, producing an extensive PIZ in optically thick filaments. Our [N II] profiles resemble the [O III] profiles measured by Baldwin, Wilson, and Whittle (1987), hence they are from the same filament population. Because [N II] $\lambda\lambda 6548$, 6583 comes from the PIZ (largely through collisional ionization of N^{0} from its ^{2}D state; CK), the filaments are indeed optically thick.

One constraint on the column length is the measurement by APBS that the extranuclear ratio [O III]/Hβ is ~ 7 for the high-velocity filaments. Single-zone, power-law, steady state photoionization models (CK; Ferland 1981) reproduce this ratio with an ionization parameter[3] Γ of $\sim 10^{-3.3}$, an upper limit because the ratio can be boosted by heating from relativistic electrons in the jet (Ferland and Mushotzky 1984). In addition, low-ionization species give a gas density $< 10^{3}$ cm^{-3} (Shields and Oke 1975), indicating a range of densities in this NLR. The kinematic model described in the next section requires $\sim 60\%$ internal obscuration to reproduce the observed line profiles. However, $\sim 90\%$ attenuation is required to reduce the flux of [O I] predicted for $\Gamma \sim 10^{3.3}$ to the observational limit. This inconsistency warns that a single-zone photoionization model is an oversimplification for this NLR (Shields and Oke 1975). So cautioned, we note that these models produce the observed nuclear [O I] $\lambda 6300$ flux with two ranges of the column density. One extreme is to truncate the PIZ to ~ 1.5 times the Strömgren column $N = c\Gamma/\alpha_{\beta} \sim 6 \times 10^{19}$ H cm^{-2} (with α_{β} the effective case B recombination coefficient). However, filaments are then only marginally opaque, and their internal attenuation is insufficient to produce the observed profile asymmetries. Columns of 2–5 $\times 10^{22}$ H cm^{-2} with the galactic dust/gas ratio can easily produce this attenuation ($N/A_V \sim 1.9 \times 10^{21}$ H cm^{-2} mag^{-1} [Bohlin, Savage, and Drake 1978]) and reduce the extranuclear fluxes from PIZ species to the observed limits. In addition, filaments with columns $\geq 10^{21}$ H cm^{-2} survive thermal conductive evaporation into the enveloping substrate, for the NLR dwell time derived from their velocities and nuclear separations (Schiano 1986). Thus current observations of this NLR are most consistent with large column densities, hence

---

[3] Γ is here defined as the ratio of ionizing photon to cloud nucleon number densities at the illuminated edge of the filament.

filament sizes $\geq 10^{16.5}$ cm and ionized masses greater than $5 \times 10^{-3}\ M_{\odot}$. The large masses show that these NLR clouds are not BLR clouds, because the typical total BLR mass of $\sim 10\ M_{\odot}$ is distributed in $\sim 10^8$ filaments.

Pressure on an outbound filament, confined in an adiabatic, constant velocity wind, decreases as R^{-2} (§ IV*c*[iv]). This causes the filament to expand and its column density to decrease as $R^{-4/3}$ until it is thin to the Lyman continuum. If the ionizing flux is nonzero as this radius is approached, species emitted by the PIZ (e.g., [N II]) will be strongly attenuated. The intensity gradients of high-velocity [O III] (BWW) and [N II] emission are similar in the NLR of NGC 1068, with both species vanishing at the same radius ($\sim 4''.5 = 320$ pc). So the filaments are apparently matter bounded (i.e., $N \geq 2$ times the Strömgren column) to the limit of their detection.

This result tightens constraints on the average filament column density hence mass, as follows. The emissivity of a collisionally excited line from each optically thick, wind-confined filament decreases as $R^{-8/3}$ below its critical density, while the measured gas density decreases as R^{-2}. If the filaments originate in the BLR, we can scale the values observed at $4''.5$ NE to the BLR radius of $\sim 0.1 L_{44}^{1/2}$ pc (Krolik and Begelman 1986), and so obtain a filament density, column density, and ionized mass of $10^{9.5}$ cm^{-3}, 6×10^{24} H cm^{-2}, and $\geq 0.06\ M_{\odot}$ (for a spherical cloud), respectively. These results should not change significantly for a transonic wind, so the large column density effectively excludes the NLR model of Krolik and Vrtilek (1984) in this galaxy because their wind requires columns less than 10^{21} H cm^{-2} for filaments from an unspecified source in the BLR. There are at least 25,000 filaments in the high-velocity regime of this NLR, consistent with the lack of substructure in the wings of the [O III] profiles at 10 km s^{-1} resolution (MP).

b) Filament Flow Field and Space Distribution

To explore the spatial and kinematical distribution of the outflow, we generated profiles from a radial flow of optically thick filaments. Our most effective constraints are the double-peaked profiles across the jet axis at the base of the NE lobe (Fig. 4*c*) and subpeak (Fig. 4*d*), where difference spectra show almost constant point-to-point flux changes but neither P Cygni patterns nor edge brightening of the broad component. (Such behavior extends to the nucleus but is obscured in the difference profiles plotted in Figs. 4*e*–4*f* by the spatially extended nuclear component. This component is subtracted from the profiles plotted in Fig. 3*b*.) Our models show that these patterns effectively exclude a power-law (including constant) emission distribution centered on the nucleus in a filled volume. By modeling independent sequences of spectra transverse to the jet axis at various points along the jet (i.e., cylindrical symmetry), we can usefully constrain the emission and velocity distributions within the emitting volume.

An overview of this restricted parameter space soon showed that split profiles and their differences are reproduced by an *enhanced gas emissivity in a thick shell about the jet axis, and an increased line-of-sight velocity with increasing distance from this axis.* Constant or decreasing *line-of-sight* velocities do not distribute flux between wings and core as observed. We find that the outflow is delineated by a small range of velocities and well-defined geometric boundaries. The volume emissivity and line-of-sight velocity distributions are well parameterized with a Gaussian displaced $\frac{1}{4}$ of the cylinder radius ($\sim 5'' = 370$ pc) from the cylinder axis, with a dispersion similar to this displacement, and a power-law $v(r) = r^{0.6}$, respectively, where r is the radius of a given shell (Fig. 8*c*). Profiles and especially their derivatives are very sensitive to deviations of more than 10% from these values at our observational resolution. Our kinematic model satisfactorily describes the split profiles in spectral sequences *c*, *d*, and *e* of Figure 4. The model suggests that internal reddening and flow parameters do not vary significantly through this range.

North-east of the nucleus, the sharp attenuation of blue relative to red wings of both our [N II] profiles and the [O III] profiles of BWW (Fig. 3*b*) is consistent with instrumental smoothing of the velocity discontinuity expected for partially opaque filaments. Similarity of the two profile species argues that extinction to the PIZ in each filament is incomplete. We crudely parameterize dispersion in the opacity of the filament population with a phase function

$$f_{\text{phase}} = 1 - \frac{\epsilon_{\text{ph}}}{2} (1 - \cos \theta_c) ,$$

where θ_c is the angle between the cloud radius vector and the cloud-observer line of sight, and ϵ_{ph} measures the amount of internal opacity. A value $\epsilon_{\text{ph}} = 0.6$ (corresponding to $A_V \sim 1.3$ mag of internal extinction) best models the observed profiles. Model profiles are somewhat sensitive to the position of the illuminating source: spectral sequences extracted perpendicular to the jet, several arcseconds outside the nucleus, are best fit with a nuclear source. To the extent that a simple phase function describes radiative transfer within individual filaments, this suggests that the jet is not the dominant ionizing source. The models show that at our instrumental resolution [N II]–emitting gas must be present within 50 pc of a prominent radio-emitting structure in the jet, the NE subpeak (WU87). However, to reproduce the observed profiles and their differences at the jet axis, emission must there be reduced to $\sim 60\%$ of its peak value at larger radii. This could arise from a combined halving of the filament filling factor and gas thermal pressure (for T near 10^4 K). If this is an ionization effect, ionization must be increased abruptly and substantially above 35 eV (i.e., above N^{++}) because the O^{++} profiles resemble N^{+}. If the dense filaments are photoionized from the nucleus, it is hard to see how their temperature can decrease at the cone axis. The flow on axis might be less thermalized than off (as for example in a jet enveloped by a shocked cocoon), thereby reducing the postshock pressure on isolated NLR filaments. However, the filaments on axis would then be accelerated relative to those off, inconsistent with our model deprojection. So we posit fewer dense NLR filaments on axis, a reduction in their area, for partial recombination from shadowing by material at smaller radii, or a combination thereof. In fact, Shields and Oke (1975) have suggested shadowing to explain fluxes from low-ionization lines in their photoionization models.

Our simple model represents with a single emissivity and velocity distribution what must be a complex, multiphase ISM. Yet it generates profiles in surprising agreement with those observed. Because we require no line broadening, the large extranuclear line widths in this NLR plausibly arise solely from geometric projection and spatial averaging of an asymmetric, large-scale flow with *no evidence for an intrinsic "turbulent" velocity in the outflowing material.* The average sound speed of NLR gas is therefore less than the velocity resolution of our profiles, ~ 140 km s^{-1}, a temperature less than $10^{6.5}$ K. So the bulk motion of the gas is highly supersonic with respect to

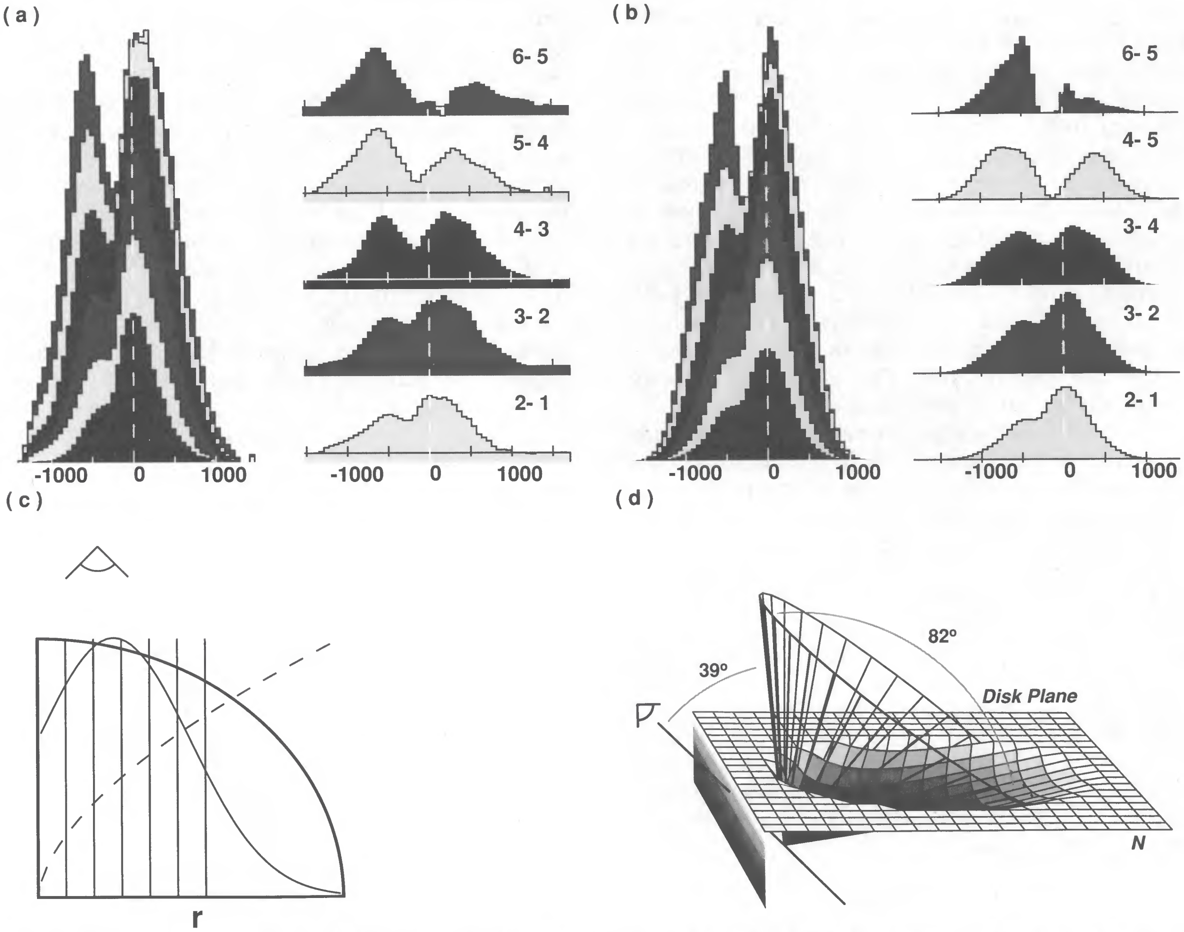

FIG. 8.—(*a*) Observed profile swath across the base of the NE radio lobe (left-hand part of *d* in Fig. 3*b*), extending SE from the jet axis (peak flux), and averaged in a (1″, 0″.5) box (along, across) the jet. The right-hand set of profiles shows spatial derivatives of the left-hand set. Velocities are relative to systemic (*dashed vertical line*). This profile structure constrains the outflow geometry. (*b*) Model profile swath across an expanding flow with a cylindrical component of motion. The line-of-sight velocities vary as $r^{0.6}$ (where r is the cylindrical radius), and the radial emission distribution is assumed to be Gaussian with centroid and dispersion 20% of the cylinder radius. Model profiles have been smoothed to our velocity resolution (~ 140 km s^{-1} FWHM) and spatial sampling (0″.48). The emitting clouds are modeled as optically thick, with 60% internal opacity (i.e., $A_V \sim 1.3$ mag of internal extinction). (*c*) A slice through the outflowing cone, showing the radial sample points (vertical bins) for (*a*) and (*b*), and the dependence of gas (volume emissivity, line-of-sight velocity) within a conical shell of this radius with (solid, dashed) lines. Note that emission drops on the jet axis. (*d*) Schematic of inferred geometry of the NE quadrant of the NLR. Plane (*c*) intersects the cone parallel to the line of sight. The cone delineates the shell with maximum emissivity, extends $\sim$4″.5 NE of the nucleus, and represents the direction of beamed kinetic and photon luminosity.

both turbulent and thermal velocities, and drag forces can become important.

In contrast to the situation in M82 (Bland and Tully 1988), the multitude of components in the extranuclear line profiles (the extended "nuclear" component in particular) and the compact spatial configuration has here prevented us from unambiguously establishing the three-dimensional distribution of the flow from the observed kinematic variations. However, it does appear that the thick shell of enhanced emissivity can be modeled as a slice through a gas distribution with a strong cylindrical component of motion. If the motion were predominantly cylindrical, material would have to expand from the jet axis to the observed radius without local line broadening by "turbulence," while exhibiting a clear dispersal in space according to its bulk velocity. While material could indeed be impulsively dispersed in the observed distribution, it seems implausible that this could occur without local line broadening at velocities of ~ 1500 km s^{-1}. Furthermore, our modeled distribution of line-of-sight velocities (Fig. 8*c*) resembles the sine function projected by a filled cone of material outflowing at roughly constant velocity. So there is clearly a definite conical component to the outflow, and we will interpret our observations under the assumption that this motion extends to small radii.

Asymmetries between spectra plotted in the left- and right-hand halves of Figure 4*c* bear on the space distribution of high- and low-velocity material in this NLR. Although the blue wings of both halves are very similar and the maximum recessional velocity is the same in both regions, material at intermediate receding velocities is attenuated in the NW (right-hand) quadrant. This may reflect an intrinsic asymmetry in the distribution of high-velocity gas within this NLR. It is also possible that opaque material is distributed between filaments in this region. As we discuss in § IV*c*[iv], the large-scale disk kinematics (Fig. 5*e*) are consistent with an inflowing population of molecular material. Although we have estimated that filaments do not completely evaporate, partial evaporation and ablation of this material in the hot ISM might release dust into the intercloud medium; radiation pressure also expels dust from filaments.

The internal opacity of the high-velocity filaments in the NE quadrant is consistent with the galactic gas/dust ratio for the inferred column density, so the opaque material plausibly lies within the filaments, and the sense of the observed asymmetry therefore confirms outflow. To orient the outflow axis, we consider the modeled profiles as a planar slice through a family of nested cones of constant velocity. The cone opening angle of maximum brightness is then effectively traced by the centroids of the deprojected emission distribution (Fig. 8*c*) along slice *d* in Figure 3*b*, and the nucleus. Our estimate, $82° \pm 3°$, is that of Bergeron, Petitjean, and Durret (1989) from the [Ne v] distribution at larger radii. The velocity centroids of (blue, red) components in the on-axis emission line profiles are (540,300) km s^{-1} with respect to systemic. For a constant-velocity, conical outflow, the brightest surfaces are then inclined 34°, 116°, respectively, to the line of sight. For an 82° opening angle, this corresponds to an axial inclination to the line of sight of 75°. The cone then has a cross section of ellipticity 0.85, and our model profiles are indeed sensitive to deviations from this value. The maximum cone opening angle may be 150°. The large-scale disk is inclined $\sim 35 \pm 5°$ from the line of sight with kinematic major axis 90° (Paper II). The jet axis at 33° P.A. is then inclined $\sim 45°$ above the disk plane. Figure 4*d* summarizes the outflow geometry in the NE quadrant. The outflow velocity is ~ 1500 km s^{-1}, and the kinetic energy exceeds 4×10^{53} ergs. The observed mass density within the NE quadrant of $\sim 100[10^{4.5}\ \mathrm{cm}^{-3}/n_e]\ M_\odot\ \mathrm{pc}^{-1}$ yields a radiant mass flux through the NLR of $0.15[10^{4.5}\ \mathrm{cm}^{-3}/n_e]\ M_\odot\ \mathrm{yr}^{-1}$ for gas at 10^4 K. As we now discuss, these large values, together with filament masses $\geq 10^{-2}\ M_\odot$, effectively exclude many proposed acceleration mechanisms.

c) Filament Acceleration

Mechanisms postulated to explain extreme velocities in the BLR (e.g., Osterbrock and Mathews 1986, and references therein) may be appropriate to the inner NLR (radii < 100 pc). The spatial extension of high-velocity gas in this NLR excludes significant orbital line broadening; alternatives are optically thick and thin filaments, moving in or out. We concentrate on mechanisms able to accelerate optically thick filaments.

i) *Jet Entrainment*

The tight alignment between jet and high-velocity gas axes suggests that the NLR filaments might be entrained interstellar clouds. Numerical studies (De Young 1986; Norman *et al.* 1982) show entrainment of thermal gas at the terminal working surface and along the jet axis as a steady state, adiabatic flow shears the enveloping ISM along its boundary. However, the jet/ISM interaction in NLRs is more likely radiative (e.g., Wilson 1989), so these simulations are irrelevant to the current situation. For NGC 1068, WU87 have argued that the low-velocity emission is gas that is cooling after passage through the bow shock. They postulate an average preshock density of $\sim 400\ \mathrm{cm}^{-3}$, based on the projected location of the present jet terminus at the edge of the dense molecular ring (MS). Our kinematic deprojection shows that the jet is inclined $\sim 45°$ to the disk plane, so the lobe height (~ 250 pc) likely exceeds the molecular scale height. In the bow-shock interpretation (§ IV*d*), we estimate that the average ambient density experienced by the propagating jet is $\sim 7\ \mathrm{cm}^{-3}$. Such low ambient densities have several consequences. First, optical emission associated with the shock near the leading edge of an ejected filament (Contini and Viegas-Aldovandi 1987, and references therein) is negligibly small even at 1500 km s^{-1} outflow velocity, so only the photoionized inner edge and PIZ emit. Second, the model of WU87 then leads to a mass-density contrast of $\sim 2 \times 10^{-3}$. As the referee has pointed out to us, radiative flows at such low jet/ambient medium density ratios have yet to be reliably simulated. We must therefore regard the question of jet entrainment as unresolved. However, our results do limit the possibilities. First, we note that high-velocity gas is much more extensively distributed than even the weakest radio flux (Fig. 3*a*). Second, numerical simulations that do include radiative cooling (albeit at much larger density contrasts, e.g., Blondin, Konigl, and Fryxell 1989) show large vortical motions around the terminal Mach disk which would be expected to generate broad emission-line profiles. However, our kinematic model argues that the flow has little intrinsic "turbulence" across the suggested jet terminus, the NE subpeak (WU87).

ii) *Entrainment around High-Pressure "Plasmons"*

The radio continuum of NGC 1068 is distributed in a string of isolated "plasmons." Pedlar, Dyson, and Unger (1985) note that the internal pressure due to relativistic electrons (as derived from minimum energy considerations) in the compact cores of these structures often greatly exceeds that of the ambient ISM, and that the ensuing expansion will shock (and so heat, accelerate, and compress) the ISM into a thin (< 10 pc thick) shell to form a confined NLR. The shocked gas cools to $\sim 10^4$ K, where its temperature is maintained by ionizing radiation from the active nucleus. The high-velocity gas would then be distributed in a filamentary sheet rather than isolated clouds. Observations of at least one NLR flow are well modeled by plasmon-driven bow shocks (Taylor *et al.* 1989; see, however, concerns raised by Wilson 1989).

How relevant are these NLR dynamics to NGC 1068? A high-pressure radio structure, the NE subpeak (WU87), is indeed observed where MP have noted the double-peaked emission-line profiles characteristic of a shocked shell. Our more complete coverage confirms that the deprojected emission distribution is enhanced in a shell. However, both its thickness (> 2″ FWHM = 150 pc) and deprojected velocity greatly exceed those expected for an expanding plasmon of internal energy 10^{55} ergs (Table I of Pedlar, Dyson, and Unger 1985). In addition, the compressed shell is expected to produce localized line broadening of several hundred km s^{-1}, yet our kinematic model argues otherwise. Although "plasmon" shocks may be important at unresolved (0″.1) scales, we feel that they are not responsible for the spatially resolved structures in the NLR.

iii) *Radiative Acceleration*

One universally applicable mechanism is radiative acceleration. Gas in the NE quadrant of NGC 1068 is exposed to a hard-spectrum photoionizing source (Bergeron, Petitjean, and Durret 1989). This photon source is likely the nucleus, and the resulting local radiative acceleration of an optically thick filament is $g_{r,\mathrm{uv}} \approx A_c L/(4\pi c R^2 M_c)$ for a filament (area, mass) of (A_c, M_c). (Penetrating X-rays are of similar importance, with the local acceleration scaling as N^{-1}.) In the absence of other forces and destructive instabilities, such filaments can be accelerated to velocities $u \approx (g_{r,\mathrm{uv}} R)^{1/2} \approx 500 N_{25}{}^{1/2}$ km s^{-1} in the BLR (N_{25} is the total column density in units of 10^{25} H cm^{-2}). However, an optically thick NLR filament is effectively stabilized against disruption by differential acceleration across its

PIZ only if a wind augments radiation pressure and its column density $\geq 10^{23}$ H cm^{-2} (Mathews and Veilleux 1989). Because the wind dominates cloud acceleration in the NLR, we now consider its consequences.

iv) *Thermal Winds*

A wind with mass efflux $\dot{M}_w \sim 0.4\ M_\odot$ yr^{-1} has been proposed in NGC 1068 (Krolik and Begelman 1986) to produce the warm medium that scatters X-ray (Toyama 1989) and broad-optical (Antonucci and Miller 1985) lines to us. Krolik and Begelman (1986) suggest that the wind material is evaporated from molecular clouds of $\sim 1\ M_\odot$ in a torus that may obscure the nuclear continuum (Antonucci and Miller 1985). The wind speed is variously estimated as 10^3–10^4 km s^{-1}, the larger value being comparable to maximum BLR velocities. The minimum wind velocity is roughly the maximum deprojected filament velocity, 1500 km s^{-1}. High-speed winds have advantages for NLR models; the wind kinetic luminosity $\dot{E}_w = \dot{M}_w V^2{}_w/2$ is then similar to the ionizing luminosity $\sim 10^{44}$ ergs s^{-1}. In particular, they may accelerate clouds of the mass estimated in § III*b* to the deprojected velocity (Schiano 1986). NLR filaments heated to 10^4 K by the active nucleus and in pressure equilibrium with a hot, rarefied confining medium (either statically, or dynamically by shocked wind material) will eventually evaporate (Cowie and McKee 1977), provided they have no magnetic field (Mathews and Capriotti 1985). The column density above which a filament survives conductive evaporation during its transit of the NLR is $N_c \approx 4 \times 10^{21}(R_{\rm kpc}/V_3)^{6/7} T_{c,4}^{-1/7} P_{c,9}^{1/7}$ H cm^{-2} (Schiano 1986), where $P_{c,9}$ is the filament thermal gas pressure (in units of 10^9 ergs cm^{-3}), $R_{\rm kpc}$ is its galactic radius, and V_3 is its velocity (units of 10^3 km s^{-1}). For this NLR we obtain $N_c \geq 6 \times 10^{21}$ H cm^{-2}, much less than that derived from relative extranuclear line strengths (to the extent that models with a single photoionized zone adequately describe this NLR). Hence the filaments survive. Shocked wind cannot emit the high-velocity flux because its cooling length $l_c \approx 10^{21} V_3{}^4/n_w$ cm greatly exceeds estimated filament sizes, or requires an unphysically large wind density n_w, hence mass efflux, for even the minimum wind velocity of ~ 1500 km s^{-1}.

The wind model of Krolik and Begelman (1986) suggests that the compact nuclear source has mass $M_H \sim 7 \times 10^6\ M_\odot$. Any central star cluster plausibly has similar mass, so gravity negligibly affects the wind and NLR filaments at observable radii. So gravitational infall of molecular clouds (e.g., CK) is not responsible for the large extranuclear line broadening in this galaxy. Instead, we now argue that massive clouds external to this NLR are *dynamically driven* to small radii. In Paper II we show from our CFHT data that the large-scale emission-line kinematics are strongly influenced by the stellar bar (MS; Thronson *et al.* 1989), by identifying the striking kinematic signature of the shocks that develop in the ISM to dissipate orbital energy when stellar orbits crowd along the bar. The bar and shocks end at the edge of the massive molecular ring (MS). The profile decomposition described in § III shows that the dynamically distinct, nonaxisymmetric component associated with these shocks (the flare) is prominent down to small radii where strong outflow motions dominate. The wind, perhaps collimated at its source by an accretion torus (Krolik and Begelman 1986), will flow freely through that part of the volume not occupied by dense filaments (i.e., most of it), until it is redirected by large-scale pressure gradients in the disk at a radius similar to the gaseous scale height (Schiano 1985) and so blows out of the disk. The flow within the disk plane stagnates (Schiano 1985) at the radius of the molecular ring; winds and clouds are here in pressure equilibrium. Collisions between molecular clouds within the "reservoir" or a cloud and the radio lobe can deflect the cloud through (what may plausibly be) the Outer Inner-Lindblad Resonance near the ring (Paper II), and into regions of radial stellar orbits. The average mass influx of $\sim 1\ M_\odot$ yr^{-1} to balance the wind efflux does not seem onerous, especially if provided in clumps the mass of typical molecular clouds. Krolik and Begelman (1986) note that molecular cloud masses are reduced by the external pressure gradient.

The kinematic response of the large-scale disk to the outflow is small (§ III*a*[ii]), so drag on the inflowing clouds is apparently insignificant. This, together with the inferred jet inclination and the limits on local profile broadening from our kinematic model, argues that most of the mass efflux is channeled away from the disk (Schiano 1985). Filaments experience either a gradual ongoing acceleration throughout the cone or impulsively near its base; the latter is indicated because hydrodynamic instabilities are intrinsically dispersive, yet our model allows no turbulence. The parent clouds are of lower density ($\sim 10^{2.5}$ cm^{-3}; MS), and so have lower emission measure. The wind is partially thermalized in a bow shock upstream of each cloud. As we showed above, the shocked wind cools inefficiently, so its flow around the cloud will be subsonic and the cloud envelope can be stripped from the core by fluid instabilities. The envelope fragments are crushed to densities of $\sim 10^3$–10^5 cm^{-3} during acceleration, until each pressure-equilibrates with the wind. Perhaps a detailed bow shock model (e.g., Taylor *et al.* 1989) can reproduce profile variations along the jet axis.

We identify the outflowing material with fragments of massive clouds and with unfragmented cloud cores that have effectively bounced off the wind and are being "catapulted" from the NLR (Smith 1984; Mobasher and Raine 1987). Figure 8*d* shows our inferred geometry for the emitting volume. In summary, the essential features of this picture are: that molecular gas at the outer boundary of the NLR is dynamically unstable to radial transport by the stellar bar; that the resulting planar influx is shielded from the brunt of the outflowing wind because the wind is largely redirected away from the disk by pressure gradients; and that the influx is ultimately scattered out of the plane and partially disrupted in the near nuclear environment. At small radii, nuclear tides and hard radiation may aid the wind in fragmenting the clouds.

An outstanding uncertainty is the fragmentation spectrum that results when parent cloud and wind interact. Recent numerical simulations (C. McKee, private communication) confirm that a blast wave shatters a dense isothermal cloud into a diffuse spray of ephemeral filaments rather than the massive fragments implied by our estimate of the column density. Simulations to extend this result to the less abrupt wind/cloud interaction, with cooling appropriate for NLR conditions, are obviously required.

d) Disk Response

So far we have limited our discussion to the brightest, most energetic emission in the NE quadrant. Other anomalous features in the NLR (Balick and Heckman 1985) will require deeper spectrophotometry to determine if they fit into the scheme developed in this paper; e.g., whether high-velocity gas in the SW quadrant (gray region in Fig. 5*d*) is also organized into a conical outflow. Figure 7 shows that this material is significantly fainter. Here we briefly discuss the low-velocity emission that is distributed in the narrow kinematic "flare" NE of the nucleus.

WU87 have interpreted this feature in the context of their high-resolution radio observations as optical emission from postshock gas at 10^4 K, generated in an ejecta-driven, radiative bow shock in the ambient ISM. They predict that its Hα luminosity is $L(\mathrm{H}\alpha) = 10^{39} n_0^2$ ergs s^{-1}, with n_0 the average density of the ambient, preshock medium in cm^{-3}. Our observed but dereddened Hα luminosity for the flare is $3(8) \times 10^{40}$ ergs s^{-1} (Table 1), corresponding to $n_0 \sim 7\ \mathrm{cm}^{-3}$. Their model predicts a bow shock velocity of several hundred km s^{-1} for a fully ionized gas at this density. The observed kinematic deviation of the flare from the large-scale bar flow, less than 50 km s^{-1}, has been substantially reduced by geometric projection. Assuming a bow shock axial inclination of 75° to the line of sight (§ IV*b*), our resulting velocity limit of less than 175 km s^{-1} is consistent with the model of WU87 for a jet speed of ≈ 4000 km s^{-1}. If improved velocity resolution reduces this limit, their model would require partial recombination of the postshock gas and so indicate shielding from, or time variability of, the beamed nuclear continuum. The major kinematic deviation from the large-scale flow pattern has amplitude 80 km s^{-1} across the bottom of the NE lobe. Because the deprojected velocity of this structure (> 100 km s^{-1}) greatly exceeds the sound speed of the ionized gas, we would expect the gas to shock; yet there is no observed flux change, suggesting that the shock effect is not dynamically significant.

V. SUMMARY

We have mapped the kinematics of collisionally excited [N II] λλ6548, 6583 across the inner 1′ diameter of the nearby Seyfert galaxy NGC 1068, using an imaging Fabry-Perot interferometer and low-noise CCD. Our complete coverage of this spatially extended NLR allows detailed study of the interaction of the outflow (Walker 1968), including the prominent collimated radio "jet" with the ionized component of the ambient ISM. After subtracting the fitted continuum level at each point, we sum our monochromatic images to generate an image equivalent to that obtained with traditional narrowband interference filters. This image shows that the NLR is aligned along the jet axis, but the correspondence is not tight. However, when our spectra are decomposed into discrete Gaussian components, specific kinematic subsystems noted by others at a few points in their long-slit data sets can be tracked across the entire NLR and often reveal a striking correlation with radio substructures. The detailed behavior of the emission-line profiles, at the few points in the NE quadrant with simple kinematics, argues that the ionized gas develops a significant component of motion perpendicular to the jet axis.

We have placed the NLR components in the context of the surrounding galaxy. In Paper II we have developed a kinematic description of the large-scale gaseous disk and have identified strong Z-shaped shocks associated with the stellar bar that indicate inward material transport from the radius of the molecular ring. In this paper we have tracked these shocks into the NLR occupied by high-velocity gas, by decomposing the emission-line profiles into discrete kinematic components. We argue that molecular clouds are transported into the wind postulated (Krolik and Begelman 1986) on independent grounds to explain the scattered nuclear broad-line (Antonucci and Miller 1985) and X-ray line (Toyama 1989) and continuum emission. Clouds are partially disrupted at small radii, and massive fragments are entrained and ejected by the wind. We argue that the radio jet is only an incidental enhancement (due to its decreased thermal pressure) in the more loosely collimated wind. The striking prominence of this NLR appears to arise from an abundant material supply (massive reservoir of molecular material and an efficient mass transporter). Both contributors to the nuclear activity are subtle in the optical continuum.

Evidently, the appearance of this NLR and that of M51 (Cecil 1988) change dramatically as the velocity resolution improves from the 1000 km s^{-1} (25 Å) passbands traditionally employed in interference imaging to the 65 km s^{-1} resolution attained with our instrument. Sharply defined, bright features exhibit sharp *kinematic* boundaries and so resemble not static, photoionized nebulae, but rather the shocked termini of hydrodynamic flows. The distribution of brightest high-velocity emission tightly correlates with the nuclear radio triple, as observed in speckle line-images at 0″.3 resolution. Therefore, down to the smallest observed scales, the spatial morphology, kinematics, and bulk of the (kinetic and turbulent) energy of the near-nuclear ionized gas are apparently driven by thermalization of a directed nuclear outflow along well-defined shocks in the ambient ISM.

What next? Multispecies extranuclear spectrophotometry will be required to establish the relative importance of beamed emission from the buried Seyfert 1 continuum and outflow/ISM shocks on the energetics of the NLR gas. To constrain filling factors, high signal-to-noise ratio line profiles of plasma diagnostics (particularly [S II] λλ6717, 6731) must be obtained across the NLR. Present weak constraints on volume and column densities lead to a hundredfold uncertainty in the energetics of the ionized gas, so line profiles from gas emitted exclusively from the partially ionized regions of filaments (e.g., [O I]) should be obtained. Finally, the high-velocity filament system and low-velocity "flare" should be studied with improved velocity resolution to better constrain their kinematic organizations; CCD-echelle profiles of [O III] λ5007 would be particularly effective.

In summary, we have shown that dynamically distinct kinematic subsystems in an NLR can be identified in emission-line profiles and that their flux and velocity variations can be mapped. Such spatially resolved maps allow plausible geometric deprojections and uniquely constrain the dynamical state of NLR filaments. The *Hubble Space Telescope* will soon image NLRs in great detail, but only second-generation instruments will produce kinematic maps.

G. C. thanks the Aspen Center for Physics for support at the 1986 Workshop on Astrophysical Jets. We are grateful to J. Ulvestad, J. Young, and P. Planesas for their radio continuum, [S III], and CO images, respectively. D. Axon, D. Clarke, D. De Young, C. McKee, and A. Schiano have shared their insights on jets and winds with us. We especially thank Andrew Wilson, our referee, for his constructive comments. This phase of our research was supported by grants NSF 86-15974 (Hawaii) and NAS8-32902 (IAS).

REFERENCES

Alloin, D., Pelat, D., Boksenberg, A., and Sargent, W. L. W. 1983, *Ap. J.*, **275**, 493 (APBS).

Antonucci, R. R. J., and Miller, J. S. 1985, *Ap. J.*, **297**, 621 (AM).

Atherton, P. D., Reay, N. K., and Taylor, K. 1986, *M.N.R.A.S.*, **216**, 17P.

Bailey, J., *et al.* 1988, *M.N.R.A.S.*, **234**, 899.

Baldwin, J. A., Wilson, A. S., and Whittle, M. 1987, *Ap. J.*, **319**, 84 (BWW).

Balick, B., and Heckman, T. M. 1985, *A.J.*, **90**, 197.

Bergeron, J., Petitjean, P., and Durret, F. 1989, *Astr. Ap.*, **213**, 61.

Bertola, F. 1966, *Pub. Obs. Padova*, **134**, 1.

Bland, J., Cecil, G., and Tully, R. B. 1990, in preparation (Paper II).

Bland, J., and Tully, R. B. 1988, *Nature*, **334**, 43.

———. 1989, *A.J.*, **98**, 723.

Blondin, J. M., Konigl, A., and Fryxell, B. A. 1989, *Ap. J.* (*Letters*), **337**, 37.

Bohlin, R. C., Savage, B. D., and Drake, J. F. 1978, *Ap. J.*, **224**, 132.

Boulesteix, J., Georgelin, Y., Marcelin, M., and Monnet, G. 1983, *Proc. SPIE*, **445**, 37.

Carroll, T. J., and Kwan, J. 1983, *Ap. J.*, **274**, 113 (CK).

Cecil, G. 1988, *Ap. J.*, **329**, 38.

Condon, J. J., Condon, M. A., Gisler, G., and Puschell, J. J. 1982, *Ap. J.*, **252**, 102.

Contini, M., and Viegas-Aldovandi, S. M. 1987, *Astr. Ap.*, **185**, 39.

Cowie, L. L., and McKee, C. F. 1977, *Ap. J.*, **211**, 135.

De Young, D. S. 1986, *Ap. J.*, **307**, 62.

Ebstein, S. M., Carleton, N. P., and Papaliolios, C. 1989, *Ap. J.*, **336**, 103.

Ferland, G. 1981, *Ap. J.*, **249**, 17.

Ferland, G., and Mushotzky, R. F. 1984, *Ap. J.*, **286**, 42.

Glaspey, J. W., Walker, G. A. H., and Stockton, A. S. 1975, *Ap. J.*, **210**, 27.

Hayes, D. S. 1970, *Ap. J.*, **159**, 165.

Kaneko, N., *et al.* 1989, *Ap. J.*, **337**, 691.

Kennicutt, R. C., and Pogge, R. W. 1990, *A.J.*, **99**, 61.

Koski, A. T. 1978, *Ap. J.*, **223**, 56.

Krolik, J. H., and Begelman, M. C. 1986, *Ap. J.* (*Letters*), **308**, L55.

Krolik, J. H., and Vrtilek, J. M. 1984, *Ap. J.*, **279**, 521.

MacKay, C. D. 1986, *Ann. Rev. Astr. Ap.*, **24**, 255.

Mathews, W. G., and Capriotti, E. R. 1985, in *Astrophysics of Active Galaxies and Quasi-Stellar Objects*, ed. J. S. Miller (Mill Valley, CA: University Science Books), p. 185.

Mathews, W. G., and Veilleux, S. 1989, *Ap. J.*, **336**, 93.

McCall, M. L. 1984, *M.N.R.A.S.*, **208**, 253.

Meaburn, J., and Pedlar, A. 1986, *Astr. Ap.*, **159**, 336 (MP).

Miller, J. S., and Mathews, W. G. 1972, *Ap. J.*, **172**, 593.

Mobasher, B., and Raine, D. J. 1987, *M.N.R.A.S.*, **228**, 159.

Myers, S. T., and Scoville, N. Z. 1987, *Ap. J.* (*Letters*), **312**, L39 (MS).

Nishimura, M., Kaneko, N., and Toyama, K. 1984, *Astr. Ap.*, **130**, 46.

Norman, M. L., Smarr, L., Winkler, K.-H. A., and Smith, M. D. 1982, *Astr. Ap.*, **113**, 285.

Osterbrock, D. E., and Mathews, W. G. 1986, *Ann. Rev. Astr. Ap.*, **24**, 171.

Pedlar, A., Dyson, J. E., and Unger, S. 1985, *M.N.R.A.S.*, **214**, 463.

Pelat, D., and Alloin, D. 1980, *Astr. Ap.*, **81**, 172 (PA).

Pierce, M. J. 1987, private communication.

Planesas, P., Scoville, N. Z., and Myers, S. T. 1989, in *The Interstellar Medium in External Galaxies*, ed. H. Thronson and D. Hollenbach (NASA Tech. Memo.), in press.

Pogge, R. W. 1988, *Ap. J.*, **328**, 519.

Richstone, D. O., and Morton, D. C. 1975, *Ap. J.*, **201**, 289.

Schiano, A. V. R. 1985, *Ap. J.*, **299**, 24.

———. 1986, *Ap. J.*, **302**, 81.

Shields, G. A., and Oke, J. B. 1975, *Ap. J.*, **197**, 5.

Smith, M. D. 1984, *M.N.R.A.S.*, **209**, 913.

Taylor, D., Dyson, J. E., Axon, D. J., and Pedlar, A. 1989, *M.N.R.A.S.*, **240**, 487.

Thronson, H. A., *et al.* 1989, *Ap. J.*, **343**, 158.

Toyama, K. 1989, in *IAU Symposium 134, Active Galactic Nuclei*, ed. D. E. Osterbrock and J. S. Miller (Dordrecht: Kluwer), p. 167.

Tully, R. B. 1988, *Nearby Galaxies Catalog* (New York: Cambridge University Press).

Ulvestad, J. S., Neff, S. G., and Wilson, A. S. 1987, *A.J.*, **93**, 22.

Walker, M. F. 1968, *Ap. J.*, **151**, 71.

Walsh, J. R. 1983, *Astr. Ap.*, **123**, 101.

Whittle, M., Pedlar, A., Meurs, E. J. A., Unger, S. W., Axon, D. J., and Ward, M. J. 1988, *Ap. J.*, **326**, 125.

Wilson, A. S. 1987, in *IAU Symposium 121, Observational Evidences of Activity in Galaxies*, ed. E. Ye Khachikian, K. J., Fricke, and J. Melnick (Dordrecht: Reidel), p. 237.

———. 1988, *Adv. Space Res.*, **8**, 27.

———. 1989, in *Proc. ESO Workshop on Extranuclear Activity in Galaxies*, ed. R. Fosbury and J. Meurs (Munich: European Southern Observatory), p. 215.

Wilson, A. S., and Heckman, T. M. 1985, in *Astrophysics of Active Galaxies and Quasi-Stellar Objects*, ed. J. S. Miller (Mill Valley, CA: University Science Books), p. 39.

Wilson, A. S., and Ulvestad, J. E. 1982, *Ap. J.*, **263**, 576.

———. 1983, *Ap. J.*, **275**, 8 (WU83).

———. 1987, *Ap. J.*, **319**, 105 (WU87).

Young, J. S., Kleinmann, S. G., and Allen, L. E. 1988, *Ap. J.* (*Letters*), **334**, L63.

JONATHAN BLAND: Department of Space Sciences and Astronomy, Rice University, Houston, TX 77251-1892

GERALD CECIL: Department of Physics and Astronomy, Phillips Hall, University of North Carolina, Chapel Hill, NC 27599

R. BRENT TULLY: Institute for Astronomy, University of Hawaii, 2680 Woodlawn Drive, Honolulu, HI 96822